



Speciation of iron(II/III) at the iron-cement interface: a review

Erich Wieland · George Dan Miron · Bin Ma · Guoqing Geng ·
Barbara Lothenbach 

Received: 27 September 2022 / Accepted: 21 January 2023
© The Author(s) 2023

Abstract Steel is used as reinforcement in construction materials and it is also an important component of cement-stabilized waste materials to be disposed of in deep geological repositories for radioactive waste. Steel corrosion releases dissolved Fe(II/III) species that can form corrosion products on the steel surface or interact with cementitious materials at the iron-cement interface. The thermodynamically stable Fe species in the given conditions may diffuse further into the adjacent, porous cement matrix and react with individual cement phases. Thus, the retention of Fe(II/III) by the hydrate assemblage of cement paste is an important process affecting the diffusive transport of the aqueous species into the cementitious materials. The diffusion of aqueous Fe(II/III) species from the

steel surface into the adjacent cementitious material coupled with the kinetically controlled formation of iron corrosion products, such as by Fe(II) oxidation, decisively determines the extension of the corrosion front. This review summarises the state-of-the-art knowledge on the interaction of ferrous and ferric iron with cement phases based on a literature survey and provides new insights and proper perspectives for future study on interaction systems of iron and cement.


Keywords Ferrous iron · Ferric iron · Steel · Cement · Thermodynamic modelling

1 Introduction

De-passivation and corrosion of steel bars in concrete can lead to considerable damage on a structural level. Reinforcement corrosion can impair the structural serviceability and load bearing capacity because of cracking and spalling of the concrete cover, loss of bonds at the steel–concrete interface and reduction of the sectional area of reinforcing steel as summarised in recent reviews [1, 2]. The Fe(II) and Fe(III) generated by the corrosion of steel are expected to affect also the mineral composition of hydrated cement in the long term. The changes in the hydrates will occur at the iron/steel–concrete interface or near to it as reported by Angst et al. [2] and illustrated in Fig. 1.

E. Wieland · G. D. Miron · B. Ma
Laboratory for Waste Management, Paul Scherrer Institut,
Villigen PSI, Switzerland

G. Geng
Department of Civil and Environmental Engineering,
National University of Singapore, Singapore 117576,
Singapore

B. Lothenbach 
Concrete & Asphalt Laboratory, Empa, Dübendorf,
Switzerland
e-mail: barbara.lothenbach@empa.ch

B. Lothenbach
Institute of Geological Sciences, University of Bern, Bern,
Switzerland



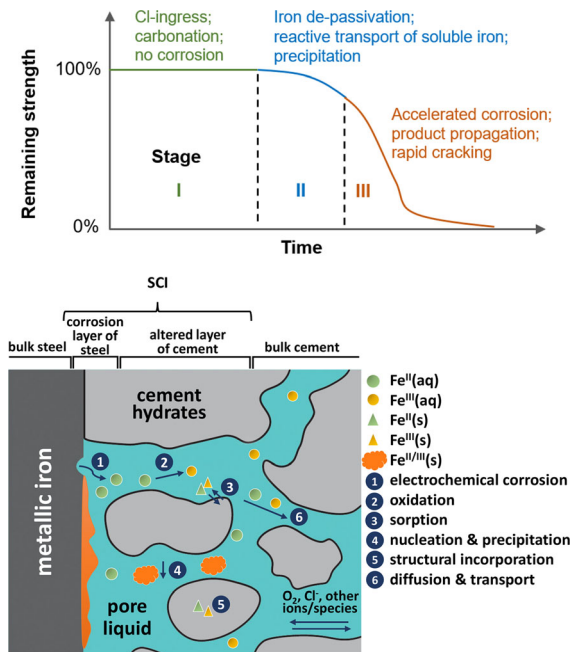


Fig. 1 Top: Simplified three-stage corrosion deterioration in reinforced concrete (curve not to scale), adapted from [15]. Bottom: Schematic illustration of the steel–concrete interface (SCI) and of the interrelated processes (labelled with numbers 1–6) governing the corrosion (adapted from Angst et al. [2])

In addition to reinforcing steel in concrete structures, metallic iron in cement can originate from ground granulated blast furnace slag (GGBFS) or non-ferrous metallurgy slag, which can contain a substantial amount of Fe(0) present as finely dispersed metallic nano- to micron-sized particles [3–5]. To date, limited information is available on the long-term fate of this nano- to micron-sized Fe(0) in alkali-activated slags or in blends with Portland cement (PC). It is conceivable that the corrosion behaviour of Fe(0) in slag cements is similar to that of reinforcing iron (and steel) bars in concrete structures, although the kinetics might be different due to the large surface area of the micron-sized granules as compared to reinforcing bars and as GGBFS can lead to reducing conditions in the pore solution [6, 7]. Studies on the corrosion of reinforcing bars in concrete show that the corrosion rate is controlled by the multiple factors, including the chemical conditions (i.e. pH, redox conditions, chloride and other elemental content of concrete pore solution, etc.), the metallography of the rebar, the pore structure of concrete and the moisture condition near the interface [8–10].

It is agreed that the corrosion of reinforced concrete takes place in three kinetic stages (Fig. 1). Chloride ingress and carbonation reaching the steel–concrete interface often mark the end of stage I, during which the steel is not corroded. In stage II, the oxidation of iron is activated, and the dissolved iron species undergo a reactive transport in the cement paste, precipitating in the pore space and/or taken up by the hydration products. When the expansive corrosion product generates sufficient micro-cracks, the concrete cover becomes much more pervious to chloride, water and oxygen, driving the degradation to stage III when the structure quickly loses its strength. The modelling of stage I has been widely reported and validated [11–14], whereas it is still very challenging to model stage II. This is largely due to the limited understanding of the initial corrosion product formation and interaction with porous cement paste. The unpredicted duration of stage II limits the decision of the best maintenance time, as it is too early to take any action in stage I, but too late in stage III.

The corrosion of iron and steel releases ferrous Fe(II) and ferric Fe(III) species, which either form corrosion products on the steel surface or diffuse into the adjacent cementitious material, thus giving rise to interaction with cement phases or, depending on solubility, to the formation of specific Fe-containing minerals [16]. Reactive transport models have been developed that allow steel corrosion and the distribution of corrosion products to be predicted in concrete structures [17, 18] and in connection with the long-term safe disposal of radioactive waste in deep geological repositories (DGR) [19–26]. Depending on the application, the models have been based on a series of parallel processes mimicking steel dissolution and interaction with adjacent materials. For example, iron dissolution, diffusion and oxidation of ferrous iron as well as precipitation of ferrous and ferric iron-containing minerals have been considered for applications in concrete structures [16–18].

The diffusion of the aqueous species is an important transport mechanism in the porous media, which is driven by the gradient in the concentration of the solutes. The molar flux due to molecular diffusion in the porous media is characterized by an apparent diffusion coefficient, which depends on the diffusion constant, the accessible porosity of the material, the geometry of the pore network (constrictivity, tortuosity) and, in the case of sorbing ions, on the sorption

properties of the ion [12, 27]. In cementitious environments, the mobility and thus the diffusion distance depend decisively on the interaction of the diffusing ion with individual cement minerals or the formation of a precipitate accommodating the ion.

Depending on the physico-chemical conditions (solution properties, availability of moisture, temperature, etc.), different types of Fe-containing cement phases and corrosion products are stable. These exhibit a wide range of properties, e.g. ranging from highly soluble to insoluble solids, and variable volumes that affect the porosity and permeability, material performance and the retention and transport of iron from the steel–concrete interface. The evolution of important chemical properties, such as redox, pH, ionic strength etc., and solid-phase parameters, such as mineralogy, porosity etc., at the steel–concrete interface is governed by the Fe-containing phases that are formed and their stability under the evolving conditions [21]. Knowledge of the interaction of ferrous and ferric iron species with cement phases and thermodynamic data on the stability of the iron-containing phases as well as on the kinetics of phase formation are therefore required to accurately model the long-term behaviour of iron/steel at the interface with cementitious materials.

The aim of this review paper is to discuss the chemical processes involving ferrous and ferric iron at the iron/steel–concrete interface based on new literature with a view to possible impacts on the long-term stability of cementitious materials. To this end, state-of-the-art knowledge on the nature of the iron corrosion products and the interaction of Fe(II) and Fe(III) with cement phases is summarised and a preliminary assessment of the long-term evolution of the iron–cement interface is undertaken.

2 Corrosion products on the steel surface

In cementitious environment, metallic iron is thermodynamically not stable and subject to corrosion. A dense oxide film on the iron/steel surface may inhibit further corrosion, which however is readily destabilized by Cl^- ions and/or decreased pH [1]. The active iron in aqueous media is described in terms of an electrochemical process involving two separate, but coupled anodic and cathodic processes proceeding simultaneously [28]. The anodic process involves the

oxidation of iron, which produces ferrous (Fe^{2+}) or ferric (Fe^{3+}) ions and releases electrons. The electrons are subsequently consumed by a cathodic process, which involves the reduction of an oxidising agent acting as electron acceptor. Overall, electrical neutrality is preserved.

In most engineered structures, including in the early phase of a DGR, the corrosion of iron/steel under aerobic conditions will initially proceed by the reduction of oxygen (electron acceptor). Under these conditions, the common corrosion products identified are Fe(III) (oxy)hydroxides and oxides. In the long term in DGRs [29–31] and near the steel surface, the redox conditions can evolve from oxidising to reducing conditions due to consumption of the available oxygen and reduction of the oxygen fugacity. In the absence of oxygen or other oxidising agents, iron corrosion involves the reduction of water, which results in the production of hydrogen and the formation of Fe(II/III) corrosion products, in particular magnetite.

The main products formed during corrosion under anaerobic conditions are magnetite (Fe_3O_4) [32, 33] and “black rust”, which is mainly composed of magnetite as well [28, 34]. The aerobic corrosion of iron and steel gives rise to the formation of Fe(III) oxyhydroxides and oxides, e.g. ferrihydrite ($\text{FeOOH}\cdot x\text{H}_2\text{O}$), lepidocrocite ($\gamma\text{-FeOOH}$) and goethite ($\alpha\text{-FeOOH}$) in concrete structures. These minerals can further crystallise to maghemite ($\gamma\text{-Fe}_2\text{O}_3$) and hematite ($\alpha\text{-Fe}_2\text{O}_3$), while magnetite (Fe(II)Fe(III)O_4) may also be present [28, 35–37]. Corrosion products have further been characterised in archaeological samples that had undergone corrosion under aerobic conditions in a natural environment over a very long period of time [38, 39]. Under these conditions, goethite ($\alpha\text{-FeOOH}$) and magnetite/maghemite ($\text{Fe}_3\text{O}_4/\gamma\text{-Fe}_2\text{O}_3$) were identified as the main corrosion products using classical laboratory techniques, such as X-ray diffraction (XRD) and Raman spectroscopy [40–43], and modern synchrotron-based micro-spectroscopic techniques [44–46] and micro X-ray diffractometric methods [5, 47].

In addition to the main corrosion products, small proportions of siderite (FeCO_3) and/or basic Fe hydroxychlorides ($\text{Fe}_2(\text{OH})_3\text{Cl}$, $\beta\text{-FeO}_{1-x}(\text{OH})_{1+x}\text{Cl}_x$) were observed. This finding is in agreement with earlier laboratory-scale studies on the formation processes of iron oxyhydroxides during the aerobic



corrosion of iron [48–50] and measurements on steel bars embedded in cementitious system over more than 60 years [51].

In chloride-bearing environments ferric akaganéite (β -FeO(OH,Cl)) and ferrous hibbingite (γ -Fe₂(OH)₃Cl) were identified [52–54]. Fe(OH)₂ is favoured with increasing pH, while the hydroxychloride phases form in neutral to slightly alkaline environments [53, 55]. In the presence of oxygen, Fe₂(OH)₃Cl is unstable in the long term and transforms into magnetite [52].

Mixed Fe(II/III)-bearing intermediates may form during partial oxidation depending on the specific conditions (solution composition, oxygen fugacity etc.). For example, if the pore water contains chloride, sulphate, and carbonate ions, phases such as “green rusts” (GR) can form [55–58]. GRs are layered double hydroxides (LDH) with mixed Fe(II/III) composition that generally form in anaerobic, neutral to alkaline systems in the presence of anions such as carbonate, sulphate, or chloride [58]. In the presence of oxygen, the ferrous corrosion products will be destabilized and depending on the solution properties, GRs will be metastable intermediate products before being transformed into stable oxide (magnetite) or oxyhydroxide phases (goethite, akaganéite, lepidocrocite) [52, 59]. Thus, the long-term stable corrosion products under aerobic conditions are goethite or magnetite. In the presence of magnesium, also stable Fe(II)- or Fe(III)-containing LDH can form [60–62] as well as LDH with mixed Fe(II/III) replacements, as recently reported in slag cements [63].

Siliceous hydrogarnet, the main Fe-containing phase in hydrated PC paste [64, 65], has also been identified as a product formed at the iron-cement interface during anaerobic iron corrosion [33]. Corrosion of steel forms a passive protecting thin film on ordinary reinforcing steel embedded in an alkaline pore solution [8]. Experimental investigations of the corrosion products formed on archaeological artefacts buried in soil, which corresponds to anaerobic corrosion in near-neutral carbonated media, were performed using both classical laboratory [36, 66–69] and synchrotron-based [70] techniques. The formation of ferrous carbonates, e.g. siderite (FeCO₃), chukanovite (Fe₂(OH)₂CO₃), and/or magnetite (Fe₃O₄) was observed depending on the local pH conditions and carbonate concentrations. Hence, the nature of the corrosion products is also influenced by the presence of carbon and sulphur species in solution, which can

lead to the formation of iron carbonates [71] and iron sulphides [72] under anaerobic conditions. Ferrous iron carbonates such as FeCO₃, Fe₂(OH)₂CO₃ and Fe₆(OH)₁₂CO₃, or the hydroxysalt chukanovite Fe₂(OH)₂CO₃ have been reported [36, 73]. However, there is evidence to suggest that under anaerobic alkaline (pH > 11) conditions at the iron/steel-cement interface and in presence of moderate carbon and sulphur concentrations, the predominant corrosion product is magnetite [74, 75].

The above compilation of selected studies illustrates that a large range of corrosion products under aerobic and anaerobic conditions has been identified, which vary depending on the chemical environment. Over long time scales of centuries and millennia, the thickness of the corrosion layer may reach a few hundred micrometres to even a few millimetres. Several layers with varying thickness have been identified at the iron/steel interface with the adjacent medium (clay, soil, cement paste, concrete etc., see Fig. 1), such as.

- (i) the metallic iron,
- (ii) a layer of corrosion products of variable porosity and consisting of various iron (oxyhydr)oxides, carbonates, and possibly sulphides, sulphates or phosphates (internal corrosion products),
- (iii) a geochemically altered layer of the adjacent medium consisting of minerals typically observed in this medium, minerals with different degrees of iron incorporation and precipitated corrosion products (external corrosion products), and
- (iv) the matrix of the adjacent medium itself [38, 39, 76].

3 Interaction of ferrous and ferric iron with cement phases

In DGR applications, the fate of ferrous and ferric iron at the interface between iron/steel and the adjacent medium, such as clay and nuclear waste glasses, has been extensively studied with the aim of assessing the long-term performance of the engineered barrier materials as a result of iron/steel corrosion [77–82]. In contrast, there is little information from in-situ corrosion studies on the Fe(II/III) species interacting



with cement phases at the steel–concrete interface [33].

At the steel–clay interface in DGR, the formation of poorly crystallised Fe-silicates was observed, indicating that a reaction between Fe(II) or Fe(III) with constituents of the clay matrix occurred [77, 78]. At the steel–glass interface, the direct contact between iron and magnetite, the main corrosion product under anaerobic conditions, with glass was reported to increase alteration of the nuclear waste glasses with subsequent implications for their long-term durability in a DGR [79–82]. It was found that the solution conditions changed significantly when magnetite was added to the system, leading to the resumption of alteration particularly in surface cracks that provided sites for the alteration. These processes resulted in the equilibrium between solution and the glass matrix being restored [82].

At the iron–cement interface, the formation of successive layers of siliceous hydrogarnet and magnetite was observed [33]. The presence of Fe-containing mineral phases with a composition characteristic of the contact medium forming a dense outer corrosion layer is expected to limit corrosion of carbon steel in anaerobic conditions in clay [83] and cementitious systems [33]. The identification of Fe-containing siliceous hydrogarnet suggests that the precipitation of secondary iron-containing cement phases and the interaction of Fe(II) and Fe(III) with existing cement phases in the cement matrix might be a common phenomenon occurring at the steel–concrete interface. The following section therefore summarises the current state of knowledge on the interaction of Fe(II) and Fe(III) with cement phases.

3.1 Uptake of ferric iron by Al-bearing cement hydrates

The hydrate assemblage of a freshly hydrated PC contains in addition to ~ 40 wt.% calcium silicate hydrate (C–S–H) and 20–25 wt.% portlandite, also 10–15 wt.% ettringite, up to 15 wt.% AFm phases, 5 wt.% Fe/Al siliceous hydrogarnet, and 2–3 wt.% other, hydrotalcite-like LDH [84–86].

Ferric iron (Fe(III)) can potentially substitute structural Al(III) in the Al-bearing hydrates such as ettringite (Aft: $\text{Ca}_6(\text{Al,Fe})_2(\text{SO}_4)_3(\text{OH})_{12}\cdot 26\text{H}_2\text{O}$), AFm phases (e.g. monosulphate $(\text{Ca}_4(\text{Al,Fe})_2(\text{SO}_4)(\text{OH})_{12}\cdot 6\text{H}_2\text{O}$, monocarbonate $(\text{Ca}_4(\text{Al,Fe})_2(\text{CO}_3)$

$(\text{OH})_{12}\cdot 5$ or $6\text{H}_2\text{O}$), hemicarbonate $(\text{Ca}_4(\text{Al,Fe})_2(\text{CO}_3)_{0.5}(\text{OH})_{13}\cdot 5.5\text{H}_2\text{O}$), Friedel's salt $(\text{Ca}_4(\text{Al,Fe})_2\text{Cl}_2(\text{OH})_{12}\cdot 4\text{H}_2\text{O})$), in hydrotalcite-like LDH $(\text{Mg}_3(\text{Al,Fe})(\text{CO}_3)_{0.5}(\text{OH})_8)$, and in siliceous hydrogarnet $(\text{Ca}_3(\text{Al,Fe})_2(\text{SiO}_4)_{0.84}(\text{OH})_{8.64})$ [61, 62, 64, 87–92]. The formation of mixed Al–Fe solid solutions has been observed for siliceous hydrogarnet, ettringite, the hydrotalcite–pyroaurite solid solution series, monosulphate, hemicarbonate and Friedel's salt but not for monocarbonate, due to the structural differences between the triclinic monocarboaluminate $\text{Ca}_4\text{Al}_2(\text{CO}_3)(\text{OH})_{12}\cdot 5\text{H}_2\text{O}$ and the trigonal monocarboferrate $\text{Ca}_4\text{Fe}_2(\text{CO}_3)(\text{OH})_{12}\cdot 6\text{H}_2\text{O}$ [87, 93].

Iron hydroxide generally precipitates initially as an amorphous or microcrystalline phase such as ferrihydrite or lepidocrocite, which recrystallises over time into thermodynamically more stable, crystalline Fe-hydroxide such as goethite (Fig. 2) or hematite. The solubility of iron hydroxide is several log units lower than those of their Al-containing counterparts, i.e. microcrystalline $\text{Al}(\text{OH})_3$ or gibbsite ($\gamma\text{-Al}(\text{OH})_3$) (Fig. 2a, b).

Experimentally derived solubility products of Fe(III)-containing hydrotalcite-like LDH phases are comparable to the corresponding Al-containing phases, while the solubility products of Fe(III)-containing ettringite, monosulphate, monocarbonate, hemicarbonate and Friedel's salt were found to be approximately 2–3 log units lower than those reported for the Al(III)-containing endmembers [90]. Furthermore, iron hydroxide and siliceous hydrogarnet are considerably more stable than their Al-containing analogues (6 log units lower solubility products) [90]. In fact, Fe/Al siliceous hydrogarnet was identified in cement paste hydrated for 10 and 50 years [65, 95] using XRD, SEM/EDX, and synchrotron-radiation based extended X-ray absorption fine structure (EXAFS) spectroscopy, while ferrihydrite has been identified during the first hours of hydration only [95].

Fe/Al siliceous hydrogarnet was observed in different cementitious environments, such as PC [95, 96] and belite–ye'elimite cements [97, 98]. However, at low belite reaction degree, where the availability of CaO is strongly limited, the possible formation of Fe-containing strätlingite has been reported [97]. The presence of Fe/Al siliceous hydrogarnet was also reported in the degraded surface layer of cement paste leached with demineralised water [99]. Fe(III)-bearing siliceous hydrogarnet was found to readily but slowly

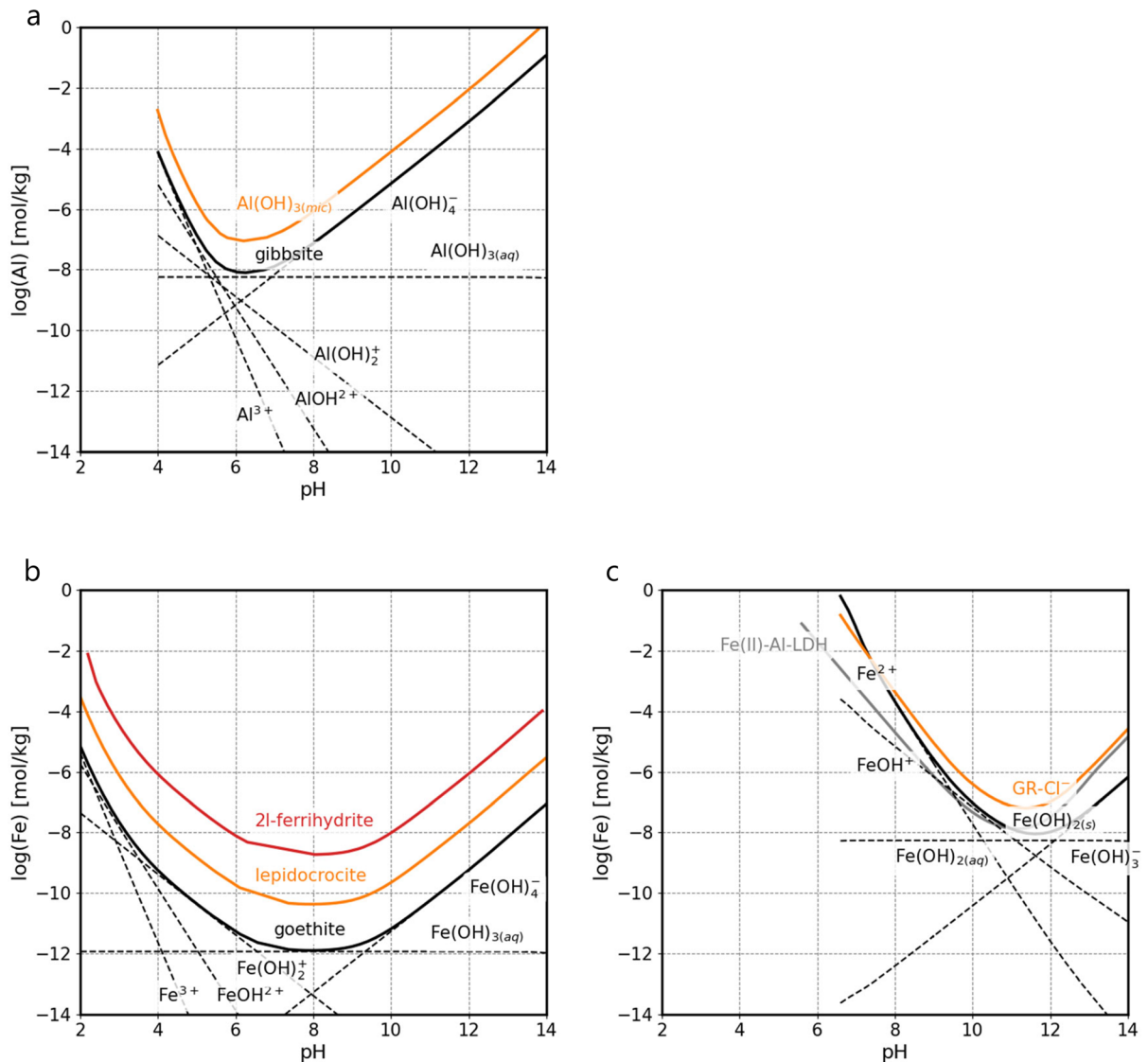


Fig. 2 Solubility at 25 °C of **a**) Al (gibbsite (γ - $\text{Al}(\text{OH})_3$), $\text{Al}(\text{OH})_3(\text{mic})$), **b**) Fe(III) (goethite (α - FeOOH), lepidocrocite (γ - FeOOH), 2-line-ferrihydrate), and **c**) Fe(II) ($\text{Fe}(\text{OH})_2(\text{s})$),

Green rust- Cl^- ($\text{Fe}(\text{III})_3\text{Fe}(\text{II})(\text{OH})_8\text{Cl}$), and Fe(II)-Al-LDH ($\text{Fe}_2\text{Al}(\text{OH})_6\text{Cl}$) calculated using thermodynamic data from Hummel and Thoenen [94] and Bhattacharya and Elzinga [60]

form at 20 °C, suggesting significant kinetic control of the formation process, while it was stable up to 110 °C [64]. At ambient temperature, the presence of Fe(III) stabilises Fe/Al siliceous hydrogarnet. Nevertheless, it only forms a poorly crystallised phase in these conditions [90, 95]. Crystalline Fe/Al siliceous hydrogarnet was identified at elevated temperature in fresh cement pastes or in cement pastes that had been aged for several years [65, 95]. Fe/Al siliceous hydrogarnet was also identified as a main product in the corrosion layers of iron in a cementitious

environment [33]. This finding supports the idea that the formation of Fe/Al siliceous hydrogarnet is thermodynamically favoured in iron- and calcium-enriched environments.

In cementitious systems with high Mg contents, e.g. due to the addition of granulated blast furnace slag or due to the presence of dolomite, Mg–Al LDHs are formed during hydration [90, 100–102]. The structure of these minerals consists of brucite-like ($\text{Mg}(\text{OH})_2$) layers, where Mg^{2+} is partially substituted by trivalent cations (Al^{3+} , Fe^{3+}), thus generating a positive charge

of the main layers, which is charge balanced by the uptake of anions in the interlayer (e.g. CO_3^{2-} , SO_4^{2-} , NO_3^- , AsO_3^-) [103–107]. The interlayer space not occupied by anions is filled with H_2O . As in the case of AFm phases, Fe^{3+} can replace Al^{3+} in hydrotalcite-like LDH phases [61, 62]. In PC, however, it appears that stabilisation of Fe^{3+} in Fe/Al siliceous hydrogarnet is thermodynamically favoured as compared to the formation of Mg-Fe(III)-LDHs [65, 95], while in low-pH cements rather the formation of ferrihydrite is expected [108].

3.2 Fe(III) bonding to C–S–H phases

Calcium silicate hydrates (C–S–H) are the most abundant cement phase in hydrated PCs and blended cements [109]. C–S–H phases take up Al(III) forming so-called C–A–S–H phases [110–118]. Aluminium is accommodated by the C–S–H phases up to a maximum Al/Si ratio ≈ 0.2 [111–113] and adopts different coordination environments in the C–S–H structure depending on the Ca/Si and Al/Si ratios [113, 119, 120]. ^{29}Si nuclear magnetic resonance (NMR) and ^{27}Al NMR spectroscopy indicate that Al is mainly coordinated in the bridging position of the silica chains in tetrahedral coordination Al^{IV} , although also minor amounts of penta- and octahedrally coordinated Al^{V} and Al^{VI} were observed [113, 114, 117, 120]. XRD further shows that the uptake of Al by C–S–H gives rise to an increase in the interlayer distance [114].

Similarly to Al(III), also the uptake of Fe(III) by C–S–H has been observed [99, 121–124]. Faucon et al. [99] and Labhasetwar et al. [122] postulated that Fe(III) is taken up via cation exchange with Ca^{2+} in the interlayer space of C–S–H phases and further concluded that Fe(III) is present in an octahedral coordination environment in the interlayer based on Mössbauer spectroscopy. More recently, Mancini et al. [123] and Siramanont et al. [124] confirmed that Fe(III) binds strongly to C–S–H phases. Sorption isotherms of Fe(III) determined by Mancini et al. [123] reveal that the sorption behaviour of Fe(III) is linear over the entire aqueous Fe concentration range for C–S–H phases with Ca/Si (C/S) ratios = 0.8, 1.2 and 1.5 (slope = 1, Fig. 3). In contrast to sorption onto TiO_2 , Fe(III) uptake by C–S–H phases was found to linearly increase over the investigated Fe(III) concentration range, implying that ferrihydrite was not a solubility-

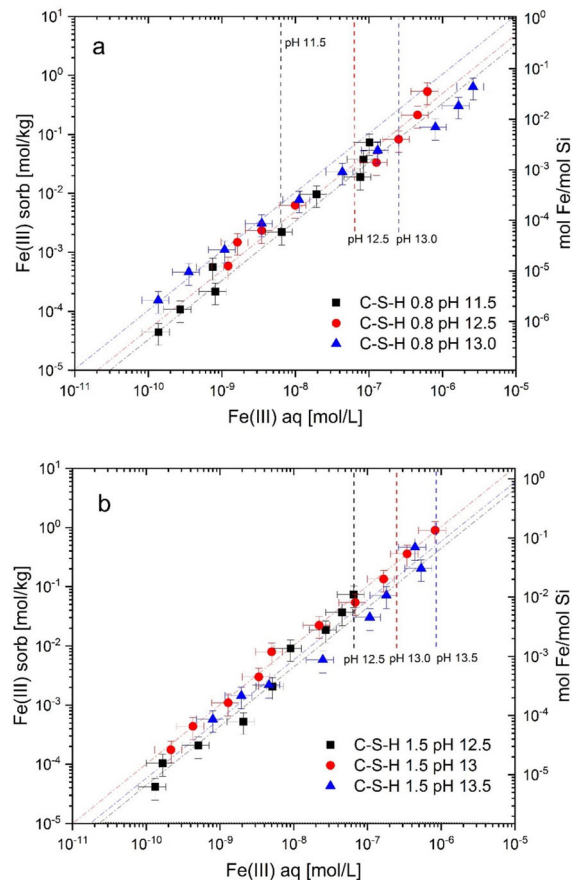


Fig. 3 Sorption isotherms of Fe(III) on C–S–H phase with Ca/Si (C/S) ratio = 0.8 (a), and C–S–H with C/S ratio = 1.5 (b). The experimental data show a linear sorption behaviour (slope = 1 of the dashed lines). Vertical dashed lines show the solubility of lepidocrocite ($\gamma\text{-FeOOH}$) at given pH values (adapted from Mancini et al. [123])

limiting phase in these systems [123]. Precipitation of amorphous $\text{Fe}(\text{OH})_3(\text{am})$ only occurred at very high Fe concentrations in the C–S–H systems as indicated by EXAFS spectroscopy [123].

The sorption isotherms in Fig. 3 indicate no or only a very weak effect of pH or of the Ca content on Fe(III) uptake by C–S–H phases as the sorption data for Fe(III) uptake by C–S–H phases with target C/S ratios = 0.8 and 1.5 agree within the experimental uncertainty in contrast to Al-uptake by C–S–H (Fig. 5). The pH determines the aqueous speciation of Fe(III); the concentration of $\text{Fe}(\text{OH})_4^-$ as well as the total Fe concentration increases with increasing pH above pH 9 (Fig. 2). Due to the increasing $\text{Fe}(\text{OH})_4^-$ concentration in the alkaline pH range, the Fe(III)

sorption on an inert oxide surface (TiO_2) was found to decrease with increasing pH in contrast to C–S–H [123].

The iron uptake by C–S–H can also be influenced by the formation of other iron-bearing phases such as siliceous hydrogarnet or ferrihydrite. If other iron-bearing phases stabilise faster, they can outcompete C–S–H for iron binding. The experimental results of Siramanont et al. [124] show that the incorporation of Fe(III) in C–S–H is highly restricted in systems where ferrihydrite initially forms and they suggest that ferrihydrite can form as an intermediate phase before siliceous hydrogarnet formation. In experiments with no precipitation of ferrihydrite, the uptake of Fe(III) in C–S–H was increased, while the formation of siliceous hydrogarnet was slowed down.

A recent literature study by Furcas et al. [59] has highlighted that the aqueous Fe(III) concentration in the presence of iron hydroxide at high pH is increased in the presence of carbonate [87, 125, 126] and silicate [64, 123] by more than a factor of 10 (Fig. 4). This increase of the total concentrations of aqueous Fe(III) in the presence of silicate and carbonate points towards the formation of presently unidentified aqueous iron(III)-hydroxide-carbonate and iron(III)-hydroxide-silicate complexes at high pH values, which have large stability constants and strongly increase the total iron concentration in solution. The data in Fig. 4

show that the increase of the Fe(III) concentration is more pronounced at high Si concentrations (low C/S ratio of C–S–H) than at low Si concentrations (high C/S ratio of C–S–H) [123].

At high C/S ratio, the interlayer space of C–S–H is occupied by Ca^{2+} ions, water molecules and possibly alkalis, while at low C/S ratios, an aqueous electrolyte containing “interlayer” space exists [127–129]. Thus, in case of a Ca(II)-Fe(III) replacement by a cation exchange process as suggested previously [99, 122], Fe(III) uptake by C–S–H phases should be lower at high Ca concentration and high C/S ratio as previously observed for the exchange of Ca^{2+} by Sr^{2+} , Ra^{2+} , Ba^{2+} , K^+ , and Na^+ on C–S–H phases [130–136]. Note that the aqueous Ca concentration is almost two orders of magnitude higher in equilibrium with a C–S–H phase with C/S ratio = 1.5 as compared to a C–S–H phase with C/S ratio = 0.8 [135, 136]. However, the Fe(III) sorption isotherms in Fig. 3 clearly reveal that Ca^{2+} has no significant effect on Fe(III) uptake, which may be related to the fact that $\text{Fe}(\text{OH})_4^-$ (and not of Fe^{3+}) predominates at pH values above pH 8 (Fig. 2), thus making a cation exchange unlikely.

In strongly alkaline solution, aqueous Fe(III) is known to have a tetrahedral coordination geometry as $[\text{Fe}(\text{OH})_4]^-$ [137]. However, at the same conditions in complex salts, Fe(III) was found to be bound preferentially in octahedral coordination [137]. The pre-

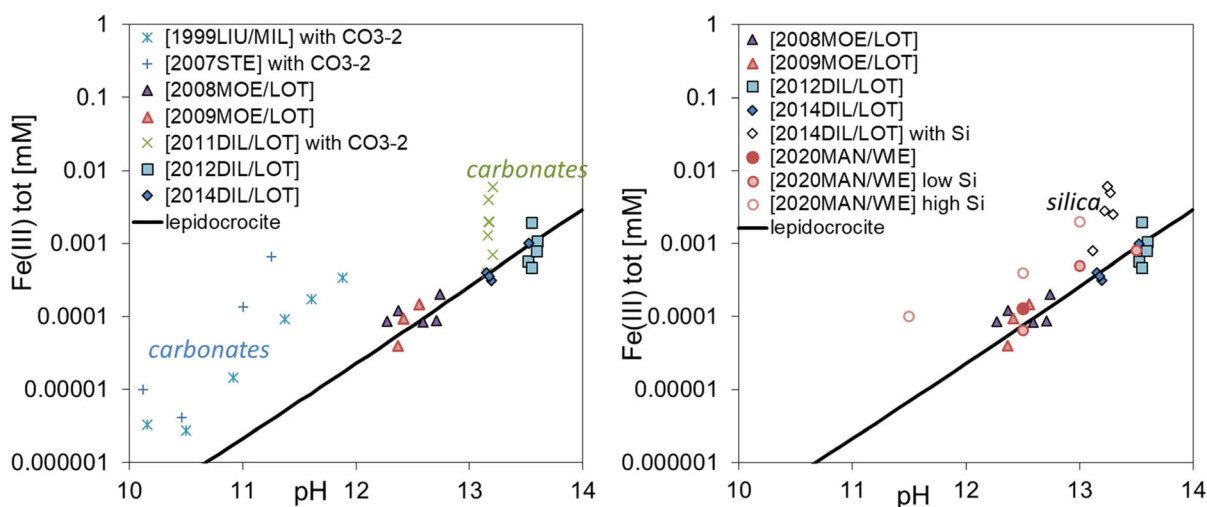


Fig. 4 Measured solubility of iron hydroxide under alkaline conditions in the presence of carbonate (left) and silica (right); experimental data collected from [64, 87, 89, 91, 92, 123, 125, 126].

The solubility of lepidocrocite ($\gamma\text{-FeOOH}$) at 20 °C (solid lines in both figures) was calculated using thermodynamic data from Hummel and Thoenen [94]



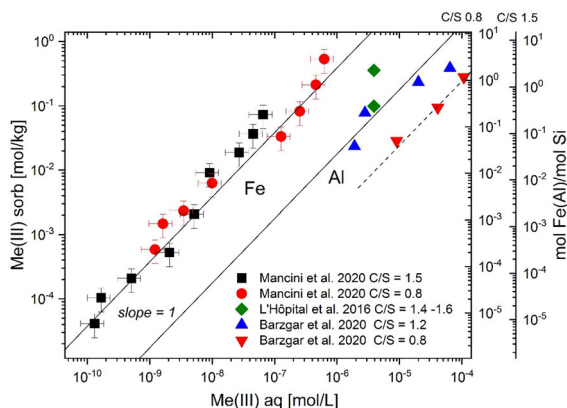


Fig. 5 Comparison of Fe(III) and Al(III) sorption isotherms on C–S–H phases with varying C/S ratios. The left y-axis relates to the sorbed Fe(III) concentration. The molar Fe/Si or Al/Si ratios of the C–S–H phases are shown on the right y-axes. The pH in the experiments was as follows: 12.5 for Fe(III) [123], 12.4–12.6 [114] and 12.47–12.96 [112] for Al(III) (modified from Mancini et al. [119])

edge features observed by Mancini et al. [123] in X-ray absorption near edge structure (XANES) spectra of Fe(III)-loaded C–S–H phases show that Fe(III) is bound in an octahedral coordination environment to C–S–H phases, thus confirming the Mössbauer observations [99, 122]. ^{29}Si NMR relaxation data show the presence of a small amount of octahedral Fe in the silica chain at high C/S C–S–H with a maximum Fe/Si of 0.001 to 0.01 [123, 124]. The structural parameters deduced from EXAFS spectroscopy support this finding [123]. Fe(III) is surrounded by around ~ 6 O in the first coordination shell in line with octahedral coordination, and ~ 4 Si and ~ 2 Ca atoms in the second coordination shell, and about 15 O atoms in the third coordination shell. Atomic distances and numbers of neighbouring atoms suggest that Fe(III) is octahedrally coordinated to Si tetrahedra of the “dreierketten” silica chains as well as to two Ca in the interlayer space of C–S–H [123].

For C–S–H phase with a low C/S ratio of 0.8, the ^{29}Si NMR data indicated that Fe(III) is not part of the silica chain, which was further supported by EXAFS spectroscopy [123]. Fe(III) is considered to form a separate secondary Ca–Si-rich phase (or clusters) on the surface of C–S–H phases based on the EXAFS data [123]. About four neighbouring Si atoms were determined at a distance of $R_{\text{Fe-Si}}$ of $\sim 3.15 \pm 0.07 \text{ \AA}$, three Ca atoms at $R_{\text{Fe-Ca}}$ of $\sim 3.19 \pm 0.05 \text{ \AA}$ and two

Fe(III) atoms located at a distance of $R_{\text{Fe-Fe}} \sim 3.34 \pm 0.05 \text{ \AA}$.

Figure 2 shows a comparison of the Fe(III) sorption data on C–S–H phases reported by Mancini et al. [123] with those for Al reported earlier [113, 114]. The Fe(III) loading is about an order of a magnitude higher than that of Al at the same aqueous concentration. Hence, Al uptake by C–S–H phases with $C/S \geq 1$ is significantly weaker as compared to Fe(III). It is noteworthy that the difference in sorption intensity is also reflected by the difference in solubility of the Al- and Fe-hydroxides in the studied pH range of 11.5–13.5 (Fig. 2). The one order higher K_d value of Fe(III) corresponds to the almost one order lower solubility of iron hydroxide. The total sorption capacity for Al on C–S–H phases, however, is higher than for Fe(III) due to the higher solubility limit of aluminium compared to iron hydroxide.

As previously discussed, Al(III) may occupy several crystallographic positions in C–A–S–H phases [113, 119, 120, 138]. At low C/S ratio, Al in tetrahedral coordination replaces Si at the bridging position of the “dreierketten” silica chains, which is not observed in the case of Fe(III). At high C/S ratio, however, Al may also be bound in octahedral coordination similar to Fe(III) in the bridging position of the silica chains stabilised by the presence of Ca^{2+} ions [119, 120]. Nevertheless, the effects of pH and Ca on Al(III) and Fe(III) uptake by C–S–H phases were found to be different [111, 112, 123], which suggests that Fe(III) is subject to a different binding mechanism than Al(III).

3.3 Uptake of Fe(II) by cement hydrates

While $\text{Fe}(\text{OH})_2$ and Fe_3O_4 are formed under anaerobic corrosion, little information is available on the interaction ferrous iron (Fe(II)) with cement phases. The formation of FeS was reported in the presence of reduced sulphur species (HS^-) [5, 6]. Hydrotalcite, a Mg–Al LDH, forms as a minor phase in cement paste and can accommodate Fe(III) replacing Al(III) in its main layer [61, 62, 106, 107, 139, 140]. Under reducing conditions, Fe(II) can partially or completely replace magnesium in Mg–Al-LDH [60, 141, 142]. Such Fe(II)-containing Mg–Al-LDH phases have also recently been observed in cements containing slags with high Fe(0) and Mg content [63], indicating that LDH phases could act as a sink for Fe(II) in

magnesium-rich cements. The Fe(II) phases are more soluble when compared to the Fe(III) phases (Fig. 2c). A difference between the two systems is the minimum solubility at around pH 8 for the Fe(III) phases and at around pH 11 for the Fe(II) phases, respectively. Figure 2c shows that the Fe(II)-Al-LDH phase is less soluble at lower pH values, while at pH > 11 Fe(OH)₂(s) is predicted to be the most stable phase. There is a potential uncertainty of at least one order of magnitude in the predicted stabilities for the LDH phases due to variability in experimental data arising from differences in sample preparation, composition, crystallinity [60]. Upon corrosion, Fe(OH)₂ and the LDH phases are predicted to be metastable and will possibly recrystallise to magnetite with time, but in the presence of ligands like Cl⁻ in the pore solution GR might be stabilised at the expense of magnetite. The stability of the GR phase is highly dependent on the Cl⁻ concentration but also on the pH and pe [59]. With increasing pH, magnetite is favoured and higher concentrations of Cl⁻ are needed to form GR. Scoping experiments by Mancini et al. [5] also indicate the possibility of a weak uptake of Fe(II) by AFm and ettringite phases as well as in C-S-H. To the authors' knowledge, no further studies on Fe(II) interaction with cement phases have been published to date. The reason might be that studies on Fe(II) interaction with cement phases are particularly challenging due to the limited stability field of Fe(II) in strongly alkaline conditions [143].

Mancini et al. [144] concluded from co-precipitation experiments with Fe(II) in C-S-H phases that partial replacement of Ca(II) by Fe(II) may occur in C-S-H phases, while complete stoichiometric substitution was not supported by the experimental data. Apparently, the large difference in the ionic radii of Ca(II) ($r = 1.08$ to 1.20 Å in VI-VIII coordination) and Fe(II) ($r = 0.69$ and 0.86 Å in VI low and high spin coordination, respectively) limits replacement of the two bivalent metal cations. Nevertheless, about 2% Ca (on a mol basis) was replaced by Fe(II) as determined from linear combination fitting of the XANES data, resulting in low Fe/Si ratios of ~ 0.02 in C-S-H 0.8 and ~ 0.05 in C-S-H 1.5. XRD studies reveal that the uptake of Fe increases the basal spacing for both C-S-H phases, similar to the effect of Al uptake in C-S-H, which also increases the basal spacing [114, 145]. Thus, the evidence is that an increase in the basal spacing, even at low Fe/Si ratio,

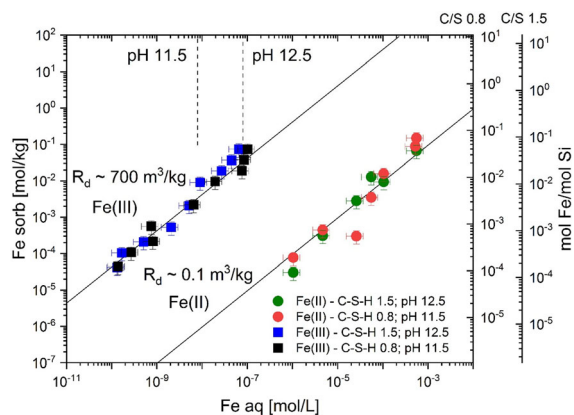


Fig. 6 Sorption isotherms of Fe(II) on C-S-H phases with C/S ratios = 0.8 and 1.5 in comparison to those of Fe(III) on the same phases [144]. The left y-axis relates to the sorbed Fe(II) concentration. The molar Fe(II)/Si ratios of the C-S-H phases are shown on the right y-axes. The vertical dashed lines indicate the calculated solubility of Fe(OH)₂ (adapted from Mancini et al. [144])

could be due to Fe(II) uptake into the interlayer of C-S-H phases as previously reported for Al(III).

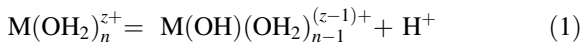
EXAFS spectroscopy studies on Fe(II)-loaded C-S-H phases show the absence of solid Fe(OH)₂(s) and linearity of the sorption isotherm of Fe(II) on the C-S-H phases up to 0.5 mM Fe(II), i.e. several log units above the expected solubility of Fe(OH)₂ of $0.9\text{--}2 \cdot 10^{-5}$ mM at pH 11.5–12.5 (Figs. 2 and 6) [144]. This could be either due to the formation of unknown aqueous Fe-Ca-Si-hydroxide complexes or due to inhibition of Fe(OH)₂(s) precipitation [59]. The isotherm measurements further reveal that Fe(II) sorption does not depend significantly on pH or the C/S ratio of the C-S-H phases, respectively, in the pH range between 11.5 and 12.5 as the sorption data agree within the experimental uncertainty, although a reduction in Fe(II) uptake at higher pH is expected due to the increasing concentration of aqueous Fe(OH)₃⁻. The uptake of Fe(II) by C-S-H phases was found to be much weaker compared to Fe(III) on the same C-S-H phases, resulting in a difference between the sorption value (K_d) of Fe(II) and Fe(III) of more than 3 orders of magnitude (Fig. 6).

Mancini et al. [144] further observed Fe(II) loadings up to 0.1 mol kg^{-1} on C-S-H phases irrespective of their C/S ratio and assumed the presence of equal proportions of surface-bound and interlayer-bound Fe(II) species on the basis of the EXAFS and XRD data. An alternative structure model was also

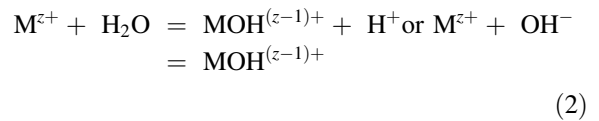
discussed based on Fe(II) incorporation into the near-surface structure of C–S–H phases, which would explain the large number of neighbouring atoms around Fe(II) (i.e. total of ~ 6 (Ca + Si) neighbours) that had been derived from EXAFS spectroscopy. In summary, Mancini et al. [144] provide a plausible interpretation by assuming that (i) Fe(II) is bonded both on the surface (formation of surface complexes) and in the interlayer at about equal quantities, (ii) both sites, i.e. surface and interlayer sites, have similar affinities for Fe(II).

3.4 Comparison between hydrolysis and sorption on C–S–H phases

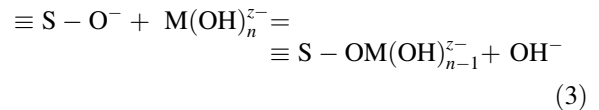
The orders of magnitude difference in the sorption values of Fe(II) and Fe(III) can tentatively be explained in terms of their different hydrolysis behaviour. In the case of hydrolysis, the O–H bonds between the metal cation and water molecules of its hydration sphere are subject to pH-dependent ionisation giving rise to the formation of hydrolysed species [146]



Thus, the initial step of hydrolysis of a cation is the formation of the first hydrolysis product, $MOH^{(z-1)+}$, and can generally be represented as follows:



The tendency of a cation to hydrolyse depends on its charge and size. For example, strongly hydrolysing cations are those that are either small (e.g. Be^{2+}) and/or highly charged (e.g. Fe^{3+} , Al^{3+}) (Fig. 7). The tendency of metal cations to hydrolyse can also be interpreted as a tendency to coordinate OH^- . A simplified view of the ligand exchange process at surface sites allows us to relate the bonding of aqueous OH^- to the metal cations to the tendency of the metal cation to coordinate to surface functional OH groups of C–S–H phases (Fig. 7). In a general way, the coordination of strongly hydrolysed metal cations (pH 12–12.5) by C–S–H phases can be described as:



$\equiv S - O^-$ represent either deprotonated OH groups bound to Ca or Si atoms on the surface or in the interlayer of C–S–H. Figure 7 shows the empirical relationship between the thermodynamic constant of the first hydrolysis reaction ($\log_{10}\beta_1^\circ$) and the distribution coefficient (K_d) of linear sorption published for metal cations sorbed onto C–S–H phases (C/S ratios 1.0–1.65) in the pH range 12–12.6. Note that the comparison does not take into account the different degrees of hydrolysis of the metal cations. For example, $Me(OH)_3^-$ species dominate in the case of Fe(II), Ni(II), Pb(II), and $Me(OH)_4^-$ species dominate in the case of Fe(III) and Al(III), while for Zn(II) and Be(II), in addition to $Me(OH)_3^-$, also $Me(OH)_4^{2-}$ is present. However, in the case of Zn(II) and Be(II), the contribution of $Me(OH)_4^{2-}$ to the distribution of the hydrolytic species at pH ~ 12 is 50% at best, which suggests that the effect of differences in speciation is presumably covered within the uncertainty range of the plotted K_d values.

The hydrolysis constants have been reported by Baes and Mesmer [146], Brown and Ekberg [147] and Hummel and Thoenen [94]. The sorption data on C–S–H phases have been reported by L'Hôpital et al. [113, 148] for Al(III), Missana et al. [132] for Ba(II), Cevirim-Papaioannou et al. [149] for Be(II), Ochs

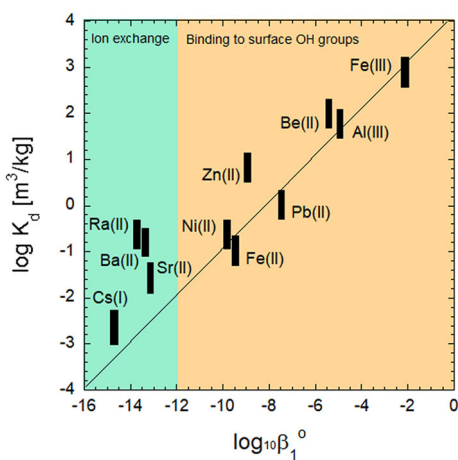


Fig. 7 Empirical relationship between the first hydrolysis constant and the distribution coefficient (K_d) of linear sorption of metal cations sorbed onto C–S–H phases (C/S ratios 1.0–1.65) in the pH range 12–12.6

et al. [150] and Missana et al. [151] for Cs(I), Mancini et al. [144] for Fe(II), Mancini et al. [123] for Fe(III), Missana et al. [152] for Ni(II), Poiteau [153] for Pb(II), Tits et al. [134] and Olmeda et al. [133] for Ra(II), Tits et al. [135] for Sr(II), and Ziegler et al. [154] for Zn(II).

It should be noted that the empirical relationship only holds for strongly hydrolysing metal cations, while it breaks down in the case of the weakly hydrolysing metal cations, such as the alkaline ($\log_{10}\beta_1^\circ$ ranging from -13.84 (Li^+) to < -14.7 (Cs^+), [147]) and alkaline earth metals ($\log_{10}\beta_1^\circ$ ranging from -12.57 (Ca^{2+}) to -13.7 (Ra^{2+}), [94]). For these metal cations, the interaction with the surface functional OH groups should be very weak according to the correlation shown in Fig. 7, although significant uptake by C-S-H phases has been observed in the case of alkaline and alkaline earth metals. Alkali and alkaline earth metal cations, which are positively charged even under high pH conditions, can compete with Ca^{2+} to compensate the negative surface charge of C-S-H by ion exchange [131]. Ion exchange based on charge compensation can be interpreted in terms of a non-specific binding in the diffuse layer (outer-sphere coordination) rather than by specific binding to OH groups (inner-sphere coordination). The former process is favourable because these ions form only weak M-OH bonds with aqueous hydroxyl ions.

The empirical relationship displayed in Fig. 7 suggests that in the case of Al, Be, Fe(II/III), Ni, Pb and Zn (and very likely other elements that hydrolyse already at low pH, such as the actinides and lanthanides), coordination to surface OH groups of the C-S-H phases (inner-sphere coordination) significantly contributes to the stabilisation of surface metal complexes.

3.5 Thermodynamic data and models for modelling iron-cement interaction

Thermodynamic properties of Fe(II/III)-bearing minerals and cement phases as well as thermodynamic models for Fe(II/III) interaction with cement phases are essential for assessing the fate of iron released during iron/steel corrosion. They serve as inputs for improved modelling tools that couple geochemical reactions and transport, which could ultimately improve our understanding of the complex chemical

processes at the interface between iron/steel and cement.

Over the past 15 years an increasing number of solubility data for Fe(III)-containing cement phases has been retrieved from synthesis, spectroscopy, thermogravimetric and solubility experiments, which recently have been compiled in the CEMDATA18 database [90]. CEMDATA18 contains the properties of several Fe(III)-bearing AFm and AFt phases, Al/Fe siliceous hydrogarnet, and LDH phases in addition to common cement hydrates such as C-S-H, AFm and AFt phases, hydrogarnet, and magnesium silicate hydrates (M-S-H). Solid solution models for AFm, AFt, and hydrogarnet are also included in the GEM-Selektor version of the CEMDATA18 database in order to account for Fe(III) uptake by these phases. Thermodynamic data for mixed Al-Fe-containing strätlingite, however, are missing, while strätlingite containing only Fe(III) was found to be thermodynamically unstable [88, 90]. Recent reviews of the solubility of iron (oxyhydr)oxides, sulphates and carbonates [147, 155, 156] complete the thermodynamic dataset for Fe(III). However, the strong increase in the measured Fe(III) concentration in equilibrium with iron hydroxide under alkaline conditions in the presence of silica and carbonate (Fig. 4, [59]) suggests the formation of as yet unidentified aqueous iron-hydroxide-carbonate and iron-hydroxide-silicon complexes.

In addition, preliminary models have been developed to describe the Fe(III) uptake by C-S-H based on the sorption isotherms reported by Mancini et al. [123]. The uptake of Fe(III) by C-S-H was modelled a) using a K_d value of $700 \text{ m}^3/\text{kg}$ for Fe(III) [5] and b) by parameterising the recently developed C-S-H solid solution model, CASH+ [131, 157] for Fe(III) on the assumption that iron can exchange at the interlayer cation sites of the tobermorite structure [21]. Fitting of the experimental data published by Mancini et al. [123] show that the model can describe very well Fe(III) uptake by C-S-H phases with different C/S ratios and at different NaOH concentrations [21]. It is intended to extend the C-S-H model to simulate Fe(III) uptake by C-A-S-H phases, i.e. Al-containing C-S-H phases, once additional experimental data on the Fe(III) uptake by C-A-S-H phases become available.

Thermodynamic data for Fe(II)-containing minerals such as magnetite, $\text{Fe}(\text{OH})_2$ and iron sulphides



have been critically reviewed recently [147, 155, 156], while only a few data are available to describe the interaction of Fe(II) with cement phases. Thermodynamic data for akaganéite (β -FeO(OH,Cl)), hibbingite ($\text{Fe}_2(\text{OH})_3\text{Cl}$), and green rust ($\text{GR}(\text{SO}_4^{2-}, \text{Cl}^-, \text{CO}_3^{2-})$) have been determined in the last years [158–160] and recently, an estimate of the solubility of Fe(II)-containing LDH (Fe(II)-Al-LDH with a formula $\text{Fe}_2\text{Al}(\text{OH})_6\text{Cl}$) has been published [60] and was considered in our calculations. The uptake of Fe(II) by C–S–H was modelled using a K_d value of $0.1 \text{ m}^3/\text{kg}$ for Fe(II) by Mancini et al. [5], while no attempt to include Fe(II) in a C–S–H model has been reported yet, while it is planned to include it in the CASH + solid-solution model [131, 157]. Thermodynamic data to describe Fe(II) uptake in other cement hydrates such as ettringite, AFm or M–S–H phases are completely missing.

The compositions of the hydrated cements in contact with seawater and fresh water were thermodynamically modelled as shown in the following section using the geochemical modelling code Gibbs Energy Minimization Selektor (GEMS) [161]. General thermodynamic data were selected from the PSI/Nagra thermodynamic database [94, 162, 163] complemented with solubility products of the cement phases from the CEMDATA18 database [90] and additional Fe(II) phases as detailed above. Note that in the modelling data presented in the following section, the formation of quartz (SiO_2), dolomite ($\text{CaMg}(\text{CO}_3)_2$), pyrite (FeS_2), goethite (α -FeOOH), and hematite (α - Fe_2O_3) in the hydrated cements was suppressed in the calculations for kinetic reasons. Note further that allowing the formation of hematite and goethite would suppress the formation of siliceous hydrogarnet ($(\text{CaO})_3(\text{Al,Fe})_2\text{O}_3(\text{SiO}_2)_{0.84}(\text{H}_2\text{O})_{4.32}$).

4 Thermodynamic modelling of iron-cement interaction

Very few studies have modelled processes at the iron/steel-cement interface and the evolution of geochemical conditions and mineral compositions at this interface. The current situation may be a consequence of the limited thermodynamic and kinetic data available on the interaction of Fe(II) and Fe(III) with cement phases. The following examples aim at providing insight into the chemical evolution at the

iron-cement interface based on the currently available thermodynamic data.

4.1 Fate of Fe(0/II/III) in iron-rich cement systems

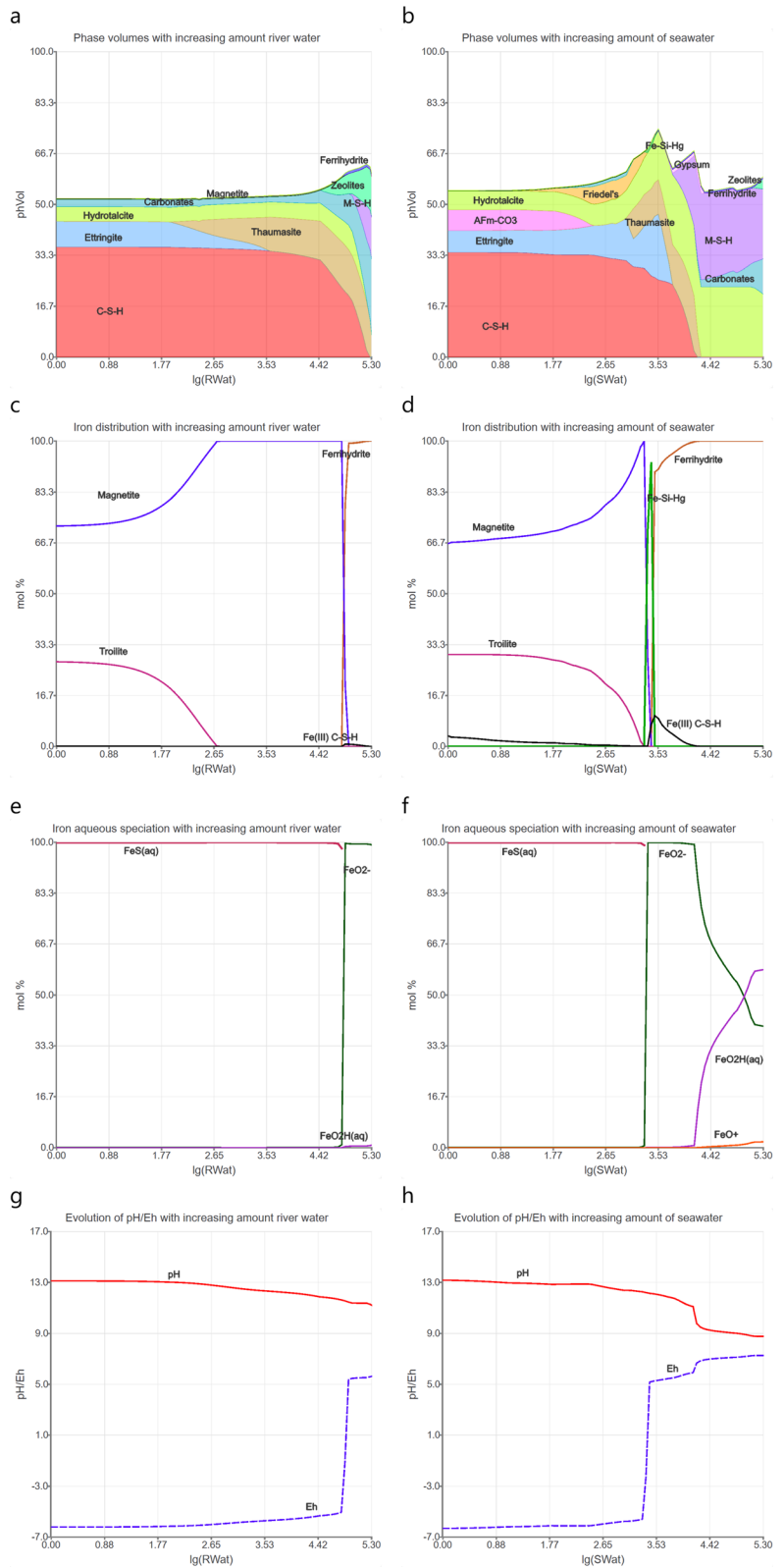
The availability of thermodynamic data allows the fate of Fe(III) in cementitious systems to be predicted and compared with experimental data. For example, thermodynamic modelling was applied to predict the time-dependent evolution of the Fe(III) speciation in PC [95, 96], blended cements [108, 164, 165] as well as in ferrite belite-ye'elimite cements [98]. In PC as well as in CaO rich blended cements and ferrite belite-ye'elimite cements, the formation of Fe/Al-siliceous hydrogarnet has been predicted [95, 96, 98] in agreement with experimental results [65, 95, 98]. The formation of Fe-ettringite is predicted by thermodynamic modelling only in the presence of a surplus of CaSO_4 [96]. In CaO-poor cements, e.g. in blended cements with a high amount of SiO_2 [7, 108] as well as in leached or carbonated surfaces [166, 167], the formation of ferrihydrite is predicted instead.

The corrosion of Fe(0) present in nano-sized particles in slag cements is relatively slow as Fe(0) has been observed after several years of reaction [3, 5]. Thermodynamic modelling of slag cements predicts reducing conditions and the formation of FeS [5, 6, 168] in agreement with the spectroscopic investigations of Mancini et al. [5] that show the presence of metallic iron along with minor proportions of iron sulphide and magnetite in alkali activated slag cements.

For slags blended PCs the formation of iron sulphide and magnetite is predicted ([5], Fig. 8) in agreement with experimental observations using standard analytical techniques in combination with synchrotron-based techniques and thermodynamic modelling [5]. Iron sulphide, iron (oxyhydr)oxides, and siliceous hydrogarnet in addition to Fe(0) have been identified in blended slag cement hydrated in contact with river water for up to 7 years. These findings suggest passivation of Fe(0) as observed on steel bars.

In contrast, no Fe(0) was observed in slag cements exposed to seawater, which indicates accelerated oxidation of Fe(0) by Cl^- . Iron sulphide, iron(II) hydroxide and oxide, iron(III) (oxyhydr)oxide and siliceous hydrogarnet have been identified as corrosion products under these conditions [5].

Fig. 8 Predicted evolution of slag-containing concrete exposed to increasing amounts (in log₁₀ scale) of river water (RWat) and North Sea seawater (SWat) based on thermodynamic modelling (modified from Mancini et al. [5]). **a, b**) hydrate assemblage, **c, d**) iron in solid phases, **e, f**) aqueous speciation of iron, and **g, h**) pH (solid line) and E_h (dashed line)



The interaction of the Fe(0)-containing slag cements with river and seawater was thermodynamically modelled as displayed in Fig. 8. Figure 8a/b show on the left the initial compositions of the hydrated cements, while on the right the gradual changes towards the surface of the concretes exposed to either river or seawater are displayed. The vicinity of the concretes to the river or seawater was simulated by increasing the amount of exposure solutions [166, 169].

Figure 8a/c/e depict the modelling for the slag-containing concrete exposed to river water. This is an update of the modelling previously reported by Mancini et al. [5] with the extension that the CASH + model [131, 157] was used, including a preliminary extension accounting for Fe(III) uptake as well as Fe(II)-containing LDH ($\text{Fe}_2\text{Al}(\text{OH})_6\text{Cl}$). C–S–H phases, ettringite, strätlingite, monocarboaluminate, hydrotalcite, and calcite are predicted to exist in the non-exposed zone at an initial pH of 13.7 (left side of Fig. 8a/c/e). Close to the surface, the formation of calcite occurs due to the ingress of carbonate present in the river water and of thaumasite ($\text{Ca}_3(\text{SiO}_3)(\text{CO}_3)(\text{SO}_4)\cdot 15\text{H}_2\text{O}$) towards the inner part, where the pH drops to 12. On the surface of the concrete, indicating more intense exposure to river water, the formation of M–S–H phases and zeolites is predicted, while C–S–H is destabilised and the pH value drops to 11. Magnetite (Fe_3O_4) and troilite (FeS) are predicted as the iron minerals that are thermodynamically stable in the non-exposed slag blended cement paste (left part in Fig. 8c), indicating conversion of Fe(0) into these minerals with time. The redox potential (E_h) of -650 mV indicates strongly reducing conditions in the unaltered part (Fig. 8e). The formation of Fe(II)-containing LDH ($\text{Fe}_2\text{Al}(\text{OH})_6\text{Cl}$) is not predicted. The formation of $\text{Fe}(\text{OH})_3$ instead of Fe_3O_4 and FeS is predicted at the surface of concrete, i.e. in areas more intensely exposed to river water. This coincides with an increase in E_h towards more oxidising conditions. Very low Fe concentrations of $0.01 \mu\text{mol/L}$ at maximum are predicted, resulting in very low Fe contents of the C–S–H phases (molar Fe(III)/Si ratio ≤ 0.001 ; molar Fe(II)/Si ratio $< 1 \times 10^{-9}$) based on the sorption data reported by Mancini et al. [123].

Figure 8 also shows the modelling results for the slag-containing concrete exposed to seawater. Again, this figure is an update of the modelling reported previously by Mancini et al. [5], extended to include

the CASH + model. In the non-exposed region of this concrete (left side of Fig. 8b/d/f), the initial composition of the hydrate assemblage is predicted to be composed of C–S–H, monocarboaluminate, hydrotalcite, and ettringite at an equilibrium pH of 13.9. Increasing exposure to seawater results in the formation of Friedel's salt ($\text{Ca}_4\text{Al}_2\text{Cl}_2(\text{OH})_{12}\cdot 4\text{H}_2\text{O}$). The pH strongly decreases (Fig. 8f) upon complete dissolution of C–S–H, indicated also by the dissolution of monocarboaluminate. The formation of ettringite, thaumasite, and gypsum occurs closer to the surface due to the presence of sulphate, carbonate, and magnesium in seawater. Friedel's salt, C–S–H phases and ettringite decompose at the surface, leading to the formation of M–S–H phases, carbonates, and hydrotalcite in agreement with the changes observed experimentally [9, 166]. The pH is ~ 9 close to the surface of concrete, which is controlled by the presence of calcite. In the hydrated, non-exposed blended cements, iron sulphides and magnetite are predicted as the thermodynamically most stable Fe-containing phases, indicating conversion of Fe(0) into these minerals with time. Fe/Al siliceous hydrogarnet seems to be stable only in a small range of seawater addition, while no Fe(II)-containing LDH is predicted. At the highest exposure to seawater, that is on the surface of the concrete where oxidising conditions dominate, ferrihydrite is the only Fe-rich phase predicted to be stable with a small amount of Fe(III) being taken up by C–S–H phases in the stability range of C–S–H. Again, the amount of Fe(II) taken up by C–S–H phases is negligibly small. The evolution of the redox conditions in the concrete exposed to seawater is comparable to that in the concrete exposed to river water. A negative E_h value is given for the pristine paste, while a strong increase occurs after complete dissolution of Fe_3O_4 and FeS .

Negative E_h values were also found in a hydrated CEM-V/A cement, which is a ternary blended cement consisting of 50 wt.% Portland cement, 25 wt.% blast furnace slag and 25 wt.% fly ash, based on the presence of reduced Fe phases and (bi)sulphides [170]. It was found that the equilibrium between half-reactions of $\text{Fe}(\text{OH})_2/\text{Fe}(\text{OH})_3$ couple and S^0/S^{2-} couple resulted in an E_h value of -450 mV at pH 13.5 [170]. This redox potential matched well with the experimental E_h value imposed by steel and the observed corrosion products in contact with the synthetic cement pore solution (pH ~ 13.5). By

applying the Nernst equation on the different corrosion product couples ($\text{Fe}^0/\text{Fe}(\text{OH})_2$, magnetite/hematite, or magnetite/goethite couple) and the redox-sensitive molecular probe (U(VI), Se(IV), Mo(VI), or Sb(V) anion) [171], it was shown that the E_h value of -450 mV is probably controlled by the amorphous $\text{Fe}(\text{OH})_2/\text{Fe}(\text{OH})_3$ or $(\text{Fe}_{1-x}, \text{Ca}_x)(\text{OH})_2/\text{Fe}(\text{OH})_3$ couple forming on the surface layer of bulk Fe(II/III) (oxyhydr)oxides. The E_h value derived from bulk magnetite/goethite couple was computed to be lower, -576 mV at $\text{pH} \sim 13.5$ [171], which is comparable to the calculated E_h values (-650 mV at $\text{pH} 13.7$) in Figs. 8e/f. The good match again confirms that the negative E_h values are mainly controlled by Fe(II/III) (oxyhydr)oxides and FeS, regardless of their origins from steel corrosion products or supplementary cementitious materials.

The thermodynamic modelling suggests that, under the given conditions and for cement compositions at thermodynamic equilibrium, Fe(III) is mainly associated with magnetite, while the extent of Fe(III) uptake by C–S–H phases is small, although Fe(III) interaction with C–S–H phases is strong and the amount of C–S–H in the concretes is large. Fe(II) is mainly associated with Fe_3O_4 and FeS, and the amount of Fe(II) accommodated by C–S–H is very low. Under reducing conditions (equilibrium with FeS and magnetite), the iron in solution is predicted to form a neutral complex with sulphur, i.e. $\text{FeS}(\text{aq})$, which dominates the ferrous iron speciation in solution. Under oxidising conditions, the iron hydrolysis species ($\text{Fe}(\text{OH})_4^-$ or FeO_2^- and $\text{Fe}(\text{OH})_3(\text{aq})$ or $\text{FeHO}_2(\text{aq})$) are the dominant chemical forms of ferric iron.

The above findings suggest a pronounced effect of the Fe(II/III) speciation on the iron mobility and support the idea that aqueous iron species originating from corrosion can be strongly retarded by the cement paste and thus will be retained close to the iron/steel-concrete interface. However, competition between iron and other cations in solution for incorporation into C–S–H might occur [123, 144].

4.2 Reactive transport and mechanical modelling of iron-cement interaction

Reactive transport modelling allows the transport and chemical reactions of multiple solutes (and gases) and their chemical interaction with materials as a function of time and space to be predicted. Reactive transport

modelling is widely used in earth sciences and in particular in conjunction with assessing the long-term performance of DGRs for radioactive waste (e.g. [172, 173]). It has become an extremely valuable tool for predicting the evolution of materials at interfaces with large chemical gradients, such as between cementitious and clayey materials (e.g. [174–177]) and at iron-clay interfaces (e.g. [19, 22, 24–26, 178]). Nevertheless, very few studies have reported the development of reactive transport models, which allow iron corrosion and the evolution of corrosion fronts in cementitious materials to be modelled in terms of coupled transport and chemical processes. For example, De Windt et al. [20] used the reactive transport code HYTEC to simulate steel corrosion in the Toarcian argillite in oxic conditions in connection with modelling oxygen gas diffusion in a disposal cell of radioactive waste. Odorowski et al. [23] published a modelling study on the effect of metallic iron on the oxidative dissolution of uranium oxide, thus accounting for iron corrosion in anoxic conditions in Callovo-Oxfordian claystone. In both studies metallic iron, goethite, magnetite, melanterite, pyrite and siderite were considered as the only possible Fe-containing solid phases, while ferrous and ferric iron-containing cement phases were not considered in the thermodynamic set-up of the modelling approaches. Reactive transport models involving iron corrosion and the distribution of corrosion products in the cementitious materials have recently been proposed [16–18, 21]. These models account for iron dissolution, ferrous ion diffusion, oxidation and precipitation of ferrous and ferric iron-containing compounds. A sensitivity analysis of the different processes revealed that the oxidation rate of ferrous to ferric iron and the matrix factors (constrictivity, tortuosity) influencing the transport of the ferrous ion are the most important parameters that can determine the distribution of corrosion products at the iron-cement interface [16]. The development of reactive transport models requires a solid understanding of the interaction of ferrous and ferric iron with cement phases and well-established thermodynamic data for the ferrous and ferric iron-containing minerals that form in cementitious environments.

Mechanical modelling of iron/steel corrosion-induced cracking in concrete have been reported since several decades ago [179–183]. Many such models needed a list of physical properties of the corrosion



product as input, such as the density, volume expansion rate, elastic modulus, creep coefficient, etc. The rate of the corrosion product formation is also often a parameter to be either fitted or presumed. Despite the highly variable (and so far not completely clear) speciation of iron at the iron-cement interface, most mechanical models seem to be able to only adopt a single phase of the hydration products throughout the corrosion process. Due to such a simplification and uncertainty of material parameters, complicated numerical/analytical modelling often does not lead to more accurate predictions than those obtained via simple, empirical models [182]. A coupled chemical-transport-mechanical modelling may provide more realistic prediction to rebar corrosion induced degradation. So far, work of this kind is very rare.

5 Conclusions

The interaction of Fe(II) and Fe(III) released in the course of iron/steel corrosion with adjacent matrices, such as glass, cement paste, etc. is a phenomenon commonly observed. This process may have a feedback on the corrosion process such as acceleration or inhibition/passivation, and further, may change the composition of the matrices at the interface with iron/steel. The formation of corrosion products at the steel-concrete interface is well known. Recent experimental studies indicate that ferrous and ferric iron generated during the course of Fe(0) corrosion may also interact with cement phases present at the interface between steel and concrete.

Fe(III) can potentially replace Al(III) in Al-containing cement phases such as AFm, AFt phases and Fe/Al siliceous hydrogarnet, which is often modelled in terms of solid solutions. Fe/Al siliceous hydrogarnet was found to be the thermodynamically most stable Fe(III)-containing phase in PC paste and it was recently identified as corrosion product formed at the iron-cement interface. At the time being, however, the impact of the formation of the Al/Fe siliceous hydrogarnet on the corrosion process has not yet been entirely clarified, i.e. whether its formation contributes to iron passivation or it may even accelerate iron corrosion. In addition to the aforementioned siliceous hydrogarnet, also C-S-H phases were found to accommodate Fe(III), predominately in the interlayer, as previously observed for Al(III). In general, it has

been observed that Fe(III)-bearing cement phases and Fe(III) (oxyhydr)oxides have a very low solubility, which results in very low Fe(III) concentrations in solution. The very low solubility of Fe(III)-bearing cement phases and the strong uptake of Fe(III) by C-S-H phases suggests strong retention of Fe(III) close to the steel-concrete interface.

In contrast to Fe(III), interaction of Fe(II) with cement phases is significantly weaker, most likely forming surface-bound complexes on AFm and AFt phases, while partial uptake of Fe(II) into the interlayer of C-S-H phases was suggested. In any case, replacement of Ca(II) by Fe(II) is very limited in cement phases, in particular in C-S-H phases.

Under the alkaline conditions ($\text{pH} > 11$) prevailing in cementitious systems, the concentrations of Fe(II) and Fe(III) ions (depending on the redox conditions) are very low with most of the iron being hydrolysed in the form of Fe(II)(OH)_3^- and Fe(III)(OH)_4^- species, respectively. However, the strong increase of measured Fe(II) and Fe(III) concentrations equilibrated with iron hydroxide in the presence of silica and carbonate indicates the presence of as yet unidentified aqueous iron-hydroxide-carbonate and iron-hydroxide-silicon complexes, which greatly increases the total iron concentration in solution and thus the transport from the corroding steel bar into the cementitious matrix. In contrast to Fe(III), Fe(II) uptake by C-S-H is much weaker, thus facilitating the mobility of Fe(II) as compared to Fe(III).

Under anaerobic conditions, the most stable corrosion product in highly alkaline conditions ($\text{pH} > 11$) is magnetite, while goethite is thermodynamically stable in oxic conditions. The formation of the stable iron oxides/hydroxides can be inhibited, depending on kinetics, temperature and local composition, resulting in the formation of different intermediate metastable phases. The presence of different ligands, such as chloride, sulphate or carbonate, can lead to the formation of complexes with iron, depending on their aqueous concentrations. For example, iron chloride species play an important role in the formation of Cl^- -containing green rust $\text{GR1(Cl}^-)$ and may enhance the solubility and transport of iron.

Thermodynamic modelling of the long-term fate of Fe(0) in slag cements exposed to fresh and seawater reveal that Fe_3O_4 and FeS are the most stable Fe-containing products resulting from Fe(0) corrosion



under anaerobic conditions. The proportion of Fe(II/III) taken up by C–S–H phases is much lower compared to Fe associated with the iron minerals. In general, it has been observed that Fe(III)-bearing cement phases and Fe oxides/hydroxides have a low solubility, which results in low Fe(III) concentrations in solution. The thermodynamic modelling of the long-term fate of Fe(0) in slag cements indicates that the formation of iron-containing minerals, such as magnetite and pyrite under anaerobic conditions, are the main sinks for iron upon release in the course of iron/steel corrosion rather than Fe(II) and Fe(III) uptake by cement phases. Nevertheless, further studies are needed to support the current, preliminary assessment, in particular to explore the possibility of ferrous and ferric iron interactions with cement phases at the iron/steel-cement interface under various geochemical conditions.

Very few studies have reported the development of reactive transport models that allow iron/steel corrosion at the iron/steel-concrete interface to be modelled by coupling transport and chemical processes. The modelling approach requires the availability of thermodynamic descriptions of the interaction of ferrous and ferric iron with cement phases (sorption, precipitation of Fe-containing cement phases). Such modelling can provide new insights with regard to the distribution of corrosion products at the iron/steel-concrete interface and their consequence for the durability of construction materials as well as the impact of steel corrosion on the engineered barriers in DGRs for radioactive waste.

Acknowledgements The authors would like to thank Göril Möschner, Belay Z. Dilnesa and Andrea Mancini for conducting the experimental research projects that led to new insights into iron-cement interaction. Thanks are extended to Rainer Dähn, Dmitrii A. Kulik, Karen Scrivener, Bernhard Wehrli and Frank Winnefeld for their scientific support and the many helpful discussions.

Funding Open Access funding provided by Lib4RI – Library for the Research Institutes within the ETH Domain: Eawag, Empa, PSI & WSL. Partial funding was received from the National Cooperative for the Disposal of Radioactive Waste (Nagra), Switzerland, and the Swiss National Science Foundation (SNF Grants No. 103546/1, 117605, 132559 and 162342). Funding for G. D. Miron was received from the European Joint Programme on Radioactive Waste Management (EURAD) in the framework of the “Assessment of Chemical Evolution of ILW and HLW Disposal Cells (ACED)” work

package (Grant Agreement No. 847593). G. Geng would like to acknowledge the Singapore MoE Grant A-0009302-01-00.

Declarations

Conflict of interest The authors declare that they have no known competing financial interests or personal relationships that could have appeared to influence the work reported in this paper.

Open Access This article is licensed under a Creative Commons Attribution 4.0 International License, which permits use, sharing, adaptation, distribution and reproduction in any medium or format, as long as you give appropriate credit to the original author(s) and the source, provide a link to the Creative Commons licence, and indicate if changes were made. The images or other third party material in this article are included in the article’s Creative Commons licence, unless indicated otherwise in a credit line to the material. If material is not included in the article’s Creative Commons licence and your intended use is not permitted by statutory regulation or exceeds the permitted use, you will need to obtain permission directly from the copyright holder. To view a copy of this licence, visit <http://creativecommons.org/licenses/by/4.0/>.

References

1. Angst U, Moro F, Geiker M, Kessler S, Beushausen H, Andrade C, Lahdensivu J, Köliö A, Imamoto K-I, von Greve-Dierfeld S, Serdar M (2020) Corrosion of steel in carbonated concrete: mechanisms, practical experience, and research priorities—a critical review by RILEM TC 281-CCC. RILEM Tech Lett 5:85–100
2. Angst UM, Geiker MR, Michel A, Gehlen C, Wong H, Isgor OB, Elsener B, Hansson CM, Francois R, Hornbostel K, Polder R, Alonso MC, Sanchez M, Correia MJ, Criado M, Sagues A, Buenfeld N (2017) The steel-concrete interface. Mater Struct 50:143
3. Bernal S, Rose V, Provis J (2014) The fate of iron in blast furnace slag particles during alkali-activation. Mater Chem Phys 146:1–5
4. Imris I, Rebolledo S, Sanchez M, Castro G, Achurra G, Hernandez F (2000) The copper losses in the slags from the El Teniente process. Can Metall Quart 39:281–289
5. Mancini A, Lothenbach B, Geng G, Grolimund D, Sanchez DF, Fakra SC, Dähn R, Wehrli B, Wieland E (2021) Iron speciation in blast furnace slag cements. Cem Concr Res 140:106287
6. Gruskovnjak A, Lothenbach B, Holzer L, Figi R, Winnefeld F (2006) Hydration of alkali-activated slag: comparison with ordinary Portland cement. Adv Cem Res 18:119–128
7. Lothenbach B, Le Saout G, Ben Haha M, Figi R, Wieland E (2012) Hydration of a low-alkali CEM III/B-SiO₂ cement (LAC). Cem Concr Res 42:410–423
8. Bertolini L, Elsener B, Pedferri P, Redaelli E, Polder RD (2013) Corrosion of steel in concrete: prevention, diagnosis, repair. Wiley-VCH, Weinheim



9. Jakobsen U, De Weerd K, Geiker M (2016) Elemental zonation in marine concrete. *Cem Concr Res* 85:12–27
10. Mundra S, Bernal SA, Provis JL (2017) Corrosion initiation of steel reinforcement in simulated alkali-activated slag pore solutions. In: 1st international conference on construction materials for sustainable future, Zadar, Croatia
11. Tang L, Nilsson L-O, Basheer PAM (2012) Resistance of concrete to chloride ingress: testing and modelling. CRC Press, Boca Raton
12. Patel RA, Phung QT, Seetharam SC, Perko J, Jacques D, Maes N, De Schutter G, Ye G, Van Breugel K (2016) Diffusivity of saturated ordinary Portland cement-based materials: a critical review of experimental and analytical modelling approaches. *Cem Concr Res* 90:52–72
13. Angst U, Elsener B, Larsen CK, Vennesland O (2009) Critical chloride content in reinforced concrete—a review. *Cem Concr Res* 39:1122–1138
14. Shafikhani M, Chidiac SE (2020) A holistic model for cement paste and concrete chloride diffusion coefficient. *Cem Concr Res* 133:106049
15. Angst U (2018) Challenges and opportunities in corrosion of steel in concrete. *Mater Struct* 51:4
16. Zhang ZD, Angst U (2021) Modelling transport and precipitation of corrosion products in cementitious materials: a sensitivity analysis. In: Chen A, Ruan X, Frangopol DM (eds) *Life-cycle civil engineering: innovation, theory and practice*. Taylor & Francis Group, London
17. Stefanoni M, Zhang Z, Angst U, Elsener B (2018) The kinetic competition between transport and oxidation of ferrous ions governs precipitation of corrosion products in carbonated concrete. *RILEM Tech Lett* 3:8–16
18. Zhang ZD, Angst U, Michel A, Jensen M (2018) An imagebased local homogenization method to model mass transport at the steel-concrete interface. In: Basheer PAM (ed) *Sixth international conference on the durability of concrete structures*. Whittles Publishing, Leeds
19. Chaparro MC, Finck N, Metz V, Geckeis H (2021) Reactive transport modelling of the long-term interaction between carbon steel and MX-80 bentonite at 25 degrees C. *Minerals* 11:1272
20. De Windt L, Marsal F, Corvisier J, Pellegrini D (2014) Modeling of oxygen gas diffusion and consumption during the oxic transient in a disposal cell of radioactive waste. *Appl Geochem* 41:115–127
21. De Windt L, Miron GD, Fabian M, Wittebroodt C (2020) First results on the thermodynamic databases and reactive transport models for steel-cement interfaces at high temperature. Deliverable 28 of the HORIZON 2020 project EURADEC Grant agreement No. 847593
22. Leupin OX, Smart NR, Zhang ZD, Stefanoni M, Angst U, Papafotiou A, Diomidis N (2021) Anaerobic corrosion of carbon steel in bentonite: an evolving interface. *Corros Sci* 187:109523
23. Odorowski M, Jegou C, De Windt L, Broudic V, Jouan G, Peugeot S, Martin C (2017) Effect of metallic iron on the oxidative dissolution of UO_2 doped with a radioactive alpha emitter in synthetic Callovian–Oxfordian groundwater. *Geochim Cosmochim Acta* 219:1–21
24. Samper J, Naves A, Montenegro L, Mon A (2016) Reactive transport modelling of the long-term interactions of corrosion products and compacted bentonite in a HLW repository in granite: uncertainties and relevance for performance assessment. *Appl Geochem* 67:42–51
25. Wersin P, Hadi J, Jenni A, Svensson D, Greneche JM, Sellin P, Leupin OX (2021) Interaction of corroding iron with eight bentonites in the alternative buffer materials field experiment (ABM2). *Minerals* 11:907
26. Wilson JC, Benbow S, Sasamoto H, Savage D, Watson C (2015) Thermodynamic and fully-coupled reactive transport models of a steel-bentonite interface. *Appl Geochem* 61:10–28
27. Crank J (1975) *The mathematics of diffusion*, 2nd edn. Oxford University Press, New York
28. Broomfield JP (2003) *Corrosion of steel in concrete: understanding, investigation and repair*, 2nd edn. Taylor & Francis, London
29. Diomidis N, Cloet V, Leupin OX, Marschall P, Poler A, Stein M (2016) Production, consumption and transport of gases in deep geological repositories according to the Swiss disposal concept. Nagra Technical Report NTB 16-03. Nagra, Wettingen
30. Duro L, Domenech C, Grive M, Roman-Ross G, Bruno J, Kallstrom K (2014) Assessment of the evolution of the redox conditions in a low and intermediate level nuclear waste repository (SFR1, Sweden). *Appl Geochem* 49:192–205
31. Wersin P, Johnson LH, Schwyn B, Berner U, Curti E (2003) Redox conditions in the near field of a repository for SF/HLW and ILW in Opalinus clay. Nagra Technical Report NTB 02-13. Nagra, Wettingen, Switzerland
32. Lopez W, Gonzalez JA (1993) Influence of the degree of pore saturation on the resistivity of concrete and the corrosion rate of steel reinforcement. *Cem Concr Res* 23:368–376
33. Pally D, Le Bescop P, Schlegel M, Miserque F, Chomat L, Neff D, L’Hostis V (2020) Corrosion behavior of iron plates in cementitious solution at 80 degrees C in anaerobic conditions. *Corros Sci* 170:108650
34. O’Donovan R, O’Rourke BD, Ruane KD, Murphy JJ (2013) Anaerobic corrosion of reinforcement. *Key Eng Mater* 569(570):1124–1131
35. Zhao Y, Jin W (2016) Steel corrosion in concrete. In: Zhao Y, Jin W (eds) *Steel corrosion-induced concrete cracking*. Butterworth-Heinemann, Oxford, pp 19–29
36. Saheb M, Gallien J-P, Descostes M, Raimbault L, Perez A, Neff D, Marsal F, Pellegrini D, Dillmann P (2014) Influence of an aerated/anoxic transient phase on the long-term corrosion of iron. *Corros Sci* 86:71–80
37. Poursae A (2016) Corrosion of steel in concrete structures. In: Poursae A (ed) *Corrosion of steel in concrete structures*. Woodhead Publishing, Duxford, pp 19–33
38. Dillmann P, Neff D, Feron D (2014) Archaeological analogues and corrosion prediction: from past to future. a review. *Corros Eng Sci Technol* 49:567–576
39. Neff D, Saheb M, Monnier J, Perrin S, Descostes M, L’Hostis V, Crusset D, Millard A, Dillmann P (2010) A review of the archaeological analogue approaches to predict the long-term corrosion behaviour of carbon steel overpack and reinforced concrete structures in the French disposal systems. *J Nucl Mater* 402:196–205

40. L'Hostis V, Neff D, Bellot-Gurlet L, Dillmann P (2009) Characterization of long-term corrosion of rebars embedded in concretes sampled on French historical buildings aged from 50 to 80 years. *Mater Corros* 60:93–98
41. Chitty WJ, Dillmann P, L'Hostis V, Lombard C (2005) Long-term corrosion resistance of metallic reinforcements in concrete—a study of corrosion mechanisms based on archaeological artefacts. *Corros Sci* 47:1555–1581
42. Monnier J, Bellot-Gurlet L, Baron D, Neff D, Guillot I, Dillmann P (2011) A methodology for Raman structural quantification imaging and its application to iron indoor atmospheric corrosion products. *J Raman Spectrosc* 42:773–781
43. Neff D, Bellot-Gurlet L, Dillmann P, Reguer S, Legrand L (2006) Raman imaging of ancient rust scales on archaeological iron artefacts for long-term atmospheric corrosion mechanisms study. *J Raman Spectrosc* 37:1228–1237
44. Dillmann P, Neff D, Mazaudier F, Hoerle S, Chevallier P, Beranger G (2002) Characterisation of iron archaeological analogues using micro diffraction under synchrotron radiation. Application to the study of long term corrosion behaviour of low alloy steels. *J Phys IIV* 12:393–408
45. Monnier J, Reguer S, Vantelon D, Dillmann P, Neff D, Guillot I (2010) X-rays absorption study on medieval corrosion layers for the understanding of very long-term indoor atmospheric iron corrosion. *Appl Phys A* 99:399–406
46. Michelin A, Drouet E, Foy E, Dynes JJ, Neff D, Dillmann P (2013) Investigation at the nanometre scale on the corrosion mechanisms of archaeological ferrous artefacts by STXM. *J Anal At Spectrom* 28:59–66. <https://doi.org/10.1039/c2ja30250k>
47. Grousset S, Kergourlay F, Neff D, Foy E, Gallias JL, Reguer S, Dillmann P, Noumowe A (2015) In situ monitoring of corrosion processes by coupled micro-XRF/micro-XRD mapping to understand the degradation mechanisms of reinforcing bars in hydraulic binders from historic monuments. *J Anal At Spectrom* 30:721–729
48. Misawa T (1973) thermodynamic consideration for Fe-H₂O system at 25 degrees C. *Corros Sci* 13:659–676
49. Misawa T, Hashimoto K, Shimodai S, (1974) Mechanism of formation of iron oxides and oxyhydroxides in aqueous solutions at room temperature. *Corros Sci* 14:131–149
50. Misawa T, Kyuno T, Suetaka W, Shimodai S (1971) Mechanism of atmospheric rusting and effect of Cu and P on rust formation of low alloy steels. *Corros Sci* 11:35–48
51. Duffo GS, Morris W, Raspini I, Saragovi C (2004) A study of steel rebars embedded in concrete during 65 years. *Corros Sci* 46:2143–2157
52. Réguer S, Mirambet F, Rémazeilles C, Vantelon D, Kergourlay F, Neff D, Dillmann P (2015) Iron corrosion in archaeological context: structural refinement of the ferrous hydroxychloride beta-Fe₂(OH)₃Cl. *Corros Sci* 100:589–598
53. Rémazeilles C, Refait P (2009) Fe(II) hydroxycarbonate Fe₂(OH)₂CO₃ (chukanovite) as iron corrosion product: synthesis and study by Fourier transform infrared spectroscopy. *Polyhedron* 28:749–756
54. Saheb M, Neff D, Dillmann P, Matthiesen H, Foy E (2008) Long-term corrosion behaviour of low-carbon steel in anoxic environment: characterisation of archaeological artefacts. *J Nucl Mater* 379:118–123
55. Nemer M, Xiong Y, Ismail A, Jang J (2011) Solubility of Fe₂(OH)₃Cl (pure-iron end-member of hibbingite) in NaCl and Na₂SO₄ brines. *Chem Geol* 280:26–32
56. Refait P, Memet J, Bon C, Sabot R, Génin J (2003) Formation of the Fe(II)–Fe(III) hydroxysulphate green rust during marine corrosion of steel. *Corros Sci* 45:833–845
57. Refait PH, Abdelmoula M, Génin JMR (1998) Mechanisms of formation and structure of green rust one in aqueous corrosion of iron in the presence of chloride ions. *Corros Sci* 40:1547–1560
58. Sagoceantsil K, Glasser F (1993) Green rust, iron solubility and the role of chloride in the corrosion of steel at high pH. *Cem Concr Res* 23:785–791
59. Furcas FE, Lothenbach B, Isgor B, Mundra S, Zhang Z, Angst UM (2022) Solubility and speciation of iron in cementitious systems. *Cem Concr Res* 151:106620
60. Bhattacharya L, Elzinga EJ (2018) A comparison of the solubility products of layered Me(II)–Al(III) hydroxides based on sorption studies with Ni(II), Zn(II), Co(II), Fe(II), and Mn(II). *Soil Syst* 2:20
61. Rozov K, Berner U, Tavio-Gueho C, Leroux F, Renaudin G, Kulik D, Diamond LW (2010) Synthesis and characterization of the LDH hydrotalcite-pyroaurite solid-solution series. *Cem Concr Res* 40:1248–1254
62. Rozov K, Berner U, Kulik D, Diamond L (2011) Solubility and thermodynamic properties of carbonate-bearing hydrotalcite-pyroaurite solid solutions with a 3:1 Mg/(Al+Fe) mole ratio. *Clays Clay Miner* 59:215–232
63. Hallet V, Pedersen MT, Lothenbach B, Winnefeld F, De Belie N, Pontikes Y (2022) Hydration of blended cement with high volume iron-rich slag from non-ferrous metallurgy. *Cem Concr Res* 151:106624
64. Dilnesa BZ, Lothenbach B, Renaudin G, Wichser A, Kulik D (2014) Synthesis and characterization of hydrogarnet Ca₃(Al_xFe_{1-x})₂(SiO₄)_y(OH)_{4(3-y)}. *Cem Concr Res* 59:96–111
65. Vespa M, Wieland E, Daehn R, Lothenbach B (2015) Identification of the thermodynamically stable Fe-containing phase in aged cement pastes. *J Am Ceram Soc* 98:2286–2294
66. Saheb M, Neff D, Descostes M, Dillmann P (2008) Inferences from a corrosion study of Iron archeological artefacts in anoxic soils. *Geochim Cosmochim Acta* 72:A818–A818
67. Saheb M, Descostes M, Neff D, Matthiesen H, Michelin A, Dillmann P (2010) Iron corrosion in an anoxic soil: comparison between thermodynamic modelling and ferrous archaeological artefacts characterised along with the local in situ geochemical conditions. *Appl Geochem* 25:1937–1948
68. Saheb M, Neff D, Demory J, Foy E, Dillmann P (2010) Characterisation of corrosion layers formed on ferrous archaeological artefacts buried in anoxic media. *Corros Eng Sci Technol* 45:381–387
69. Saheb M, Neff D, Bellot-Gurlet L, Dillmann P (2011) Raman study of a deuterated iron hydroxycarbonate to assess long-term corrosion mechanisms in anoxic soils. *J Raman Spectrosc* 42:1100–1108



70. Leon Y, Saheb M, Drouet E, Neff D, Foy E, Leroy E, Dynes JJ, Dillmann P (2014) Interfacial layer on archaeological mild steel corroded in carbonated anoxic environments studied with coupled micro and nano probes. *Corros Sci* 88:23–35
71. Matthiesen H, Hilbert LR, Gregory DJ (2003) Siderite as a corrosion product on archaeological iron from a water-logged environment. *Stud Conserv* 48:183–194
72. Bai PP, Zheng SQ, Zhao H, Ding Y, Wu J, Chen CF (2014) Investigations of the diverse corrosion products on steel in a hydrogen sulfide environment. *Corros Sci* 87:397–406
73. King F (2008) Corrosion of carbon steel under anaerobic conditions in a repository for SF and HLW in Opalinus clay. Nagra Technical Report NTB 08-12. Nagra, Wettingen
74. Kursten B, Druyts F, Macdonald DD, Smart NR, Gens R, Wang L, Weetjens E, Govaerts J (2011) Review of corrosion studies of metallic barrier in geological disposal conditions with respect to Belgian Supercontainer concept. *Corros Eng Sci Technol* 46:91–97
75. Smart NR (2009) Corrosion behavior of carbon steel radioactive waste packages: a summary review of Swedish and U.K. research. *Corrosion* 65:195–212
76. Saheb M, Marsal F, Matthiesen H, Neff D, Dillmann P, Pellegrini D (2011) Fluctuation of redox conditions in radioactive waste disposal cell: characterisation of corrosion layers formed on archaeological analogues. *Corros Eng Sci Technol* 46:199–204
77. Schlegel M, Necib S, Dumas S, Blanc C, Foy E, Trcera N, Romaine A (2016) Microstructural characterization of carbon steel corrosion in clay borehole water under anoxic and transient acidic conditions. *Corros Sci* 109:126–144
78. Schlegel M, Necib S, Dumas S, Labat M, Blanc C, Foy E, Linard Y (2018) Corrosion at the carbon steel-clay borehole water interface under anoxic alkaline and fluctuating temperature conditions. *Corros Sci* 136:70–90
79. Dillmann P, Gin S, Neff D, Gentaz L, Rebiscoul D (2016) Effect of natural and synthetic iron corrosion products on silicate glass alteration processes. *Geochim Cosmochim Acta* 172:287–305
80. Michelin A, Burger E, Leroy E, Foy E, Neff D, Benzerara K, Dillmann P, Gin S (2013) Effect of iron metal and siderite on the durability of simulated archeological glassy material. *Corros Sci* 76:403–414
81. Michelin A, Burger E, Rebiscoul D, Neff D, Bruguier F, Drouet E, Dillmann P, Gin S (2013) Silicate glass alteration enhanced by iron: origin and long-term implications. *Environ Sci Technol* 47:750–756
82. Neill L, Gin S, Ducasse T, De Echave T, Fournier M, Jollivet P, Gourgiotis A, Wall NA (2017) Various effects of magnetite on international simple glass (ISG) dissolution: implications for the long-term durability of nuclear glass. *Mater Degrad* 1:1
83. Leon Y, Dillmann P, Neff D, Schlegel M, Foy E, Dynes J (2017) Interfacial layers at a nanometre scale on iron corroded in carbonated anoxic environments. *RSC Adv* 7:20101–20115
84. De Weerd K, Ben Haha M, Le Saout G, Kjellsen KO, Justnes H, Lothenbach B (2011) Hydration mechanisms of ternary Portland cements containing limestone powder and fly ash. *Cem Concr Res* 41:279–291
85. Lothenbach B, Winnefeld F (2006) Thermodynamic modelling of the hydration of Portland cement. *Cem Concr Res* 36:209–226
86. Lothenbach B, Le Saout G, Gallucci E, Scrivener K (2008) Influence of limestone on the hydration of Portland cements. *Cem Concr Res* 38:848–860
87. Dilnesa BZ, Lothenbach B, Le Saout G, Renaudin G, Mesbah A, Filinchuk Y, Wichser A, Wieland E (2011) Iron in carbonate containing AFm phases. *Cem Concr Res* 41:311–323
88. Dilnesa BZ (2012) Fe-containing hydrates and their fate during cement hydration: thermodynamic data and experimental study. PhD thesis, Ecole Polytechnique Fédérale de Lausanne (EPFL), Lausanne
89. Dilnesa BZ, Lothenbach B, Renaudin G, Wichser A, Wieland E (2012) Stability of monosulfate in the presence of iron. *J Am Ceram Soc* 95:3305–3316
90. Lothenbach B, Kulik D, Matschei T, Balonis M, Baquerizo L, Dilnesa B, Miron G, Myers R (2019) Cemdata 18: a chemical thermodynamic database for hydrated Portland cements and alkali-activated materials. *Cem Concr Res* 115:472–506
91. Möschner G, Lothenbach B, Rose J, Ulrich A, Figi R, Kretzschmar R (2008) Solubility of Fe-ettringite ($\text{Ca}_6[\text{Fe}(\text{OH})_6]_2(\text{SO}_4)_3 \cdot 26\text{H}_2\text{O}$). *Geochim Cosmochim Acta* 72:1–18
92. Möschner G, Lothenbach B, Winnefeld F, Ulrich A, Figi R, Kretzschmar R (2009) Solid solution between Al-ettringite and Fe-ettringite ($\text{Ca}_6[\text{Al}_{1-x}\text{Fe}_x(\text{OH})_6]_2(\text{SO}_4)_3 \cdot 26\text{H}_2\text{O}$). *Cem Concr Res* 39:482–489
93. Renaudin G, Mesbah A, Dilnesa BZ, Francois M, Lothenbach B (2015) Crystal chemistry of iron containing cementitious AFm layered hydrates. In: Ruby C (ed) Green rust and related iron containing compounds: structure, redox properties and environmental applications. Bentham, Hilversum, pp 184–193
94. Hummel W, Thoenen T (2021) The PSI chemical thermodynamic data base 2020. Nagra Technical Report NTB 21-03, Nagra, Wettingen
95. Dilnesa BZ, Wieland E, Lothenbach B, Dähn R, Scrivener KL (2014) Fe-containing phases in hydrated cements. *Cem Concr Res* 58:45–55
96. Elakneswaran Y, Noguchi N, Matumoto K, Morinaga Y, Chabayashi T, Kato H, Nawa T (2019) Characteristics of ferrite-rich Portland cement: Comparison with ordinary Portland cement. *Front Mater* 6:97
97. Chitvoranund N, Lothenbach B, Londono-Zuluaga D, Winnefeld F, Scrivener K (2023) Influence of temperature on phase assemblages of belite-ye’elimite cement. *Cem Conc Res (in preparation)*
98. Morin V, Termkhajornkit P, Huet B, Pham G (2017) Impact of quantity of anhydrite, water to binder ratio, fineness on kinetics and phase assemblage of belite-ye’elimite-ferrite cement. *Cem Concr Res* 99:8–17
99. Faucon P, LeBescop P, Adenot F, Bonville P, Jacquinet JF, Pineau F, Felix B (1996) Leaching of cement: study of the surface layer. *Cem Concr Res* 26:1707–1715
100. Bernal S, Nicolas R, Myers R, de Gutiérrez R, Puertas F, van Deventer J, Provis J (2014) MgO content of slag controls phase evolution and structural changes induced by



- accelerated carbonation in alkali-activated binders. *Cem Concr Res* 57:33–43
101. Machner A, Zajac M, Ben Haha M, Kjellsen KO, Geiker MR, De Weerd K (2018) Stability of the hydrate phase assemblage in Portland composite cements containing dolomite and metakaolin after leaching, carbonation, and chloride exposure. *Cem Concr Comp* 89:89–106
102. Richardson I, Brough A, Groves G, Dobson C (1994) The characterization of hardened alkali-activated blast-furnace slag pastes and the nature of the calcium silicate hydrate (C–S–H) phase. *Cem Concr Res* 24:813–829
103. Bernard E, Zucha WJ, Lothenbach B, Mäder U (2022) Stability of hydrotalcite (Mg–Al layered double hydroxide) in presence of different anions. *Cem Concr Res* 152:106674
104. Paikaray S, Hendry M (2013) In situ incorporation of arsenic, molybdenum, and selenium during precipitation of hydrotalcite-like layered double hydroxides. *Appl Clay Sci* 77–78:33–39
105. Paikaray S, Hendry M, Essilfie-Dughan J (2013) Controls on arsenate, molybdate, and selenate uptake by hydrotalcite-like layered double hydroxides. *Chem Geol* 345:130–138
106. Paikaray S, Essilfie-Dughan J, Hendry M (2018) Ionic substitution of Mg^{2+} for Al^{3+} and Fe^{3+} with octahedral coordination in hydroxides facilitate precipitation of layered double hydroxides. *Geochim Cosmochim Acta* 220:217–234
107. Paikaray S, Hendry M (2014) Formation and crystallization of Mg^{2+} - Fe^{3+} - SO_4^{2-} - CO_3^{2-} -type anionic clays. *Appl Clay Sci* 88–89:111–122
108. Lothenbach B, Rentsch D, Wieland E (2014) Hydration of a silica fume blended low-alkali shotcrete cement. *Phys Chem Earth* 70–71:3–16
109. Lothenbach B, Scrivener K, Hooton RD (2011) Supplementary cementitious materials. *Cem Concr Res* 41:1244–1256
110. Andersen M, Jakobsen H, Skibsted J (2003) Incorporation of aluminum in the calcium silicate hydrate (C–S–H) of hydrated Portland cements: A high-field Al-27 and Si-29 MAS NMR investigation. *Inorg Chem* 42:2280–2287
111. Barzgar S, Lothenbach B, Tarik M, Di Giacomo A, Ludwig C (2020) The effect of sodium hydroxide on Al uptake by calcium silicate hydrates (C–S–H). *J Colloid Interf Sci* 572:246–256
112. Barzgar S, Tarik M, Ludwig C, Lothenbach B (2021) The effect of equilibration time on Al uptake in C–S–H. *Cem Concr Res* 144:106438
113. L'Hôpital E, Lothenbach B, Kulik D, Scrivener K (2016) Influence of calcium to silica ratio on aluminium uptake in calcium silicate hydrate. *Cem Concr Res* 85:111–121
114. L'Hôpital E, Lothenbach B, Le Saout G, Kulik D, Scrivener K (2015) Incorporation of aluminium in calcium-silicate-hydrates. *Cem Concr Res* 75:91–103
115. Myers R, L'Hôpital E, Provis J, Lothenbach B (2015) Effect of temperature and aluminium on calcium (aluminum)silicate hydrate chemistry under equilibrium conditions. *Cem Concr Res* 68:83–93
116. Pardal X, Pochard I, Nonat A (2009) Experimental study of Si–Al substitution in calcium-silicate-hydrate (C–S–H) prepared under equilibrium conditions. *Cem Concr Res* 39:637–643
117. Pardal X, Brunet F, Charpentier T, Pochard I, Nonat A (2012) Al-27 and Si-29 solid-state NMR characterization of calcium-aluminosilicate-hydrate. *Inorg Chem* 51:1827–1836
118. Richardson I, Brough A, Brydson R, Groves G, Dobson C (1993) Location of aluminum insubstituted calcium silicate hydrate (C–S–H) gels as determined by Si-29 and Al-27 NMR and EELS. *J Am Ceram Soc* 76:2285–2288
119. Mohamed AK, Moutzouri P, Berruyer P, Walder BJ, Siramanont J, Harris M, Negroni M, Galmarini SC, Parker SC, Scrivener KL, Emsley L, Bowen P (2020) The atomic-level structure of cementitious calcium aluminate silicate hydrate. *J Am Chem Soc* 142:11060–11071
120. Yang SY, Yan Y, Lothenbach B, Skibsted J (2021) Incorporation of sodium and aluminum in cementitious calcium-alumina-silicate-hydrate C–(A)–S–H phases studied by Na-23, Al-27, and Si-29 MAS NMR spectroscopy. *J Phys Chem C* 125:27975–27995
121. Faucon P, Jacquinet JF, Adenot F, Virlet J, Petit JC (1996) Influence of the degraded surface layer on the long-term behavior of cement pastes. *Mater Res Soc Symp Proc* 465:295–302
122. Labhasetwar N, Shrivastava O, Medikov Y (1991) Mössbauer study on iron-exchanged calcium silicate hydrate— $Ca_{5-x}Fe_xSi_6O_{18}H_2 \cdot nH_2O$. *J Solid State Chem* 93:82–87
123. Mancini A, Wieland E, Geng G, Dähn R, Skibsted J, Wehrli B, Lothenbach B (2020) Fe(III) uptake by calcium silicate hydrates. *Appl Geochem* 113:104460
124. Siramanont J, Walder BJ, Emsley L, Bowen P (2021) Iron incorporation in synthetic precipitated calcium silicate hydrates. *Cem Concr Res* 142:106365
125. Liu XW, Millero FJ (1999) The solubility of iron hydroxide in sodium chloride solutions. *Geochim Cosmochim Acta* 63:3487–3497
126. Stefansson A (2007) Iron(III) hydrolysis and solubility at 25 degrees C. *Environ Sci Technol* 41:6117–6123
127. Bonaccorsi E, Merlino S, Kampf A (2005) The crystal structure of tobermorite 14 A (Plombierite), a C–S–H phase. *J Am Ceram Soc* 88:505–512
128. Chen JJ, Thomas JJ, Taylor HFW, Jennings HM (2004) Solubility and structure of calcium silicate hydrate. *Cem Concr Res* 34:1499–1519
129. Richardson IG (2004) Tobermorite/jennite- and tobermorite/calcium hydroxide-based models for the structure of C–S–H: applicability to hardened pastes of tricalcium silicate, beta-dicalcium silicate, Portland cement, and blends of Portland cement with blast-furnace slag, metakaolin, or silica fume. *Cem Concr Res* 34:1733–1777
130. Lothenbach B, Nonat A (2015) Calcium silicate hydrates: Solid and liquid phase composition. *Cem Concr Res* 78:57–70
131. Miron GD, Kulik D, Yan Y, Tits J, Lothenbach B (2022) Parameterization of C–S–H–(N)–(K) sublattice solid solution model for alkali uptake. *Cem Concr Res* 152:106667
132. Missana T, Garcia-Gutiérrez M, Mingarro M, Alonso U (2017) Analysis of barium retention mechanisms on calcium silicate hydrate phases. *Cem Concr Res* 93:8–16



133. Olmeda J, Missana T, Grandia F, Grivé M, Garcia-Gutiérrez M, Mingarro M, Alonso U, Colas E, Henocq P, Munier I, Robinet J (2019) Radium retention by blended cement pastes and pure phases (C–S–H and C–A–S–H gels): experimental assessment and modelling exercises. *Appl Geochem* 105:45–54
134. Tits J, Iijima K, Wieland E, Kamei G (2006) The uptake of radium by calcium silicate hydrates and hardened cement paste. *Radiochim Acta* 94:637–643
135. Tits J, Wieland E, Muller CJ, Landesman C, Bradbury MH (2006) Strontium binding by calcium silicate hydrates. *J Colloid Interf Sci* 300:78–87
136. Yan YR, Yang SY, Miron GD, Collings IE, L'Hopital E, Skibsted J, Winnefeld F, Scrivener K, Lothenbach B (2022) Effect of alkali hydroxide on calcium silicate hydrate (C–S–H). *Cem Concr Res* 151:106957
137. Sipos P, Zeller D, Kuzmann E, Vertes A, Homonnay Z, Walczak M, Canton SE (2008) The structure of Fe(III) ions in strongly alkaline aqueous solutions from EXAFS and Mossbauer spectroscopy. *Dalton Trans.* <https://doi.org/10.1039/b806937a>
138. Renaudin G, Russias J, Leroux F, Cau-dit-Coumes C, Frizon F (2009) Structural characterization of C–S–H and C–A–S–H samples-Part II: Local environment investigated by spectroscopic analyses. *J Solid State Chem* 182:3320–3329
139. Curtius H, Kaiser G, Rozov K, Neumann A, Dardenne K, Bosbach D (2013) Preparation and characterization of Fe-, Co-, and Ni-containing Mg–Al-layered double hydroxides. *Clays Clay Miner* 61:424–439
140. Gomez M, Hendry M, Elouatik S, Essilfie-Dughan J, Paikaray S (2014) Fe(II)(aq) uptake of Mg(II)–Al(III)/Fe(III)–SO₄/CO₃ HTLCs under alkaline conditions: adsorption and solid state transformation mechanisms. *RSC Adv* 4:60112–60113
141. Kameda T, Kondo E, Yoshioka T (2014) Preparation of Mg–Al layered double hydroxide doped with Fe²⁺ and its application to Cr(VI) removal. *Sep Purif Technol* 122:12–16
142. Zhong Y, Yang Q, Luo K, Wu XQ, Li XM, Liu Y, Tang WW, Zeng GM, Peng B (2013) Fe(II)–Al(III) layered double hydroxides prepared by ultrasound-assisted coprecipitation method for the reduction of bromate. *J Hazard Mater* 250:345–353
143. Brookins DG (1988) Eh–pH diagrams for geochemistry. Springer, Berlin
144. Mancini A, Wieland E, Geng G, Lothenbach B, Wehrli B, Dahn R (2021) Fe(II) interaction with cement phases: method development, wet chemical studies and X-ray absorption spectroscopy. *J Colloid Interface Sci* 588:692–704
145. Renaudin G, Russias J, Leroux F, Frizon F, Cau-Dit-Coumes C (2009) Structural characterization of C–S–H and C–A–S–H samples-Part I: long-range order investigated by Rietveld analyses. *J Solid State Chem* 182:3312–3319
146. Baes CF, Mesmer RE (1976) The hydrolysis of cations. Wiley, New York
147. Brown PL, Ekberg C (2016) Hydrolysis of metal ions. Wiley-VCH Verlag, Weinheim
148. Yan Y, Ma B, Miron GD, Kulik DA, Scrivener K, Lothenbach B (2022) Al uptake in calcium silicate hydrate and the effect of alkali hydroxide. *Cem Concr Res* 162:106957
149. Cevirim-Papaioannou N, Androniuk I, Han S, Mouheb NA, Gaboreau S, Um W, Gaona X, Altmaier M (2021) Sorption of beryllium in cementitious systems relevant for nuclear waste disposal: Quantitative description and mechanistic understanding. *Chemosphere* 282:131094
150. Ochs M, Mallants D, Wang L (2016) Radionuclide and metal sorption on cement and concrete. Springer, Cham
151. Missana T, Garcia-Gutiérrez M, Mingarro M, Alonso U (2018) Comparison between cesium and sodium retention on calcium–silicate–hydrate (C–S–H) phases. *Appl Geochem* 98:36–44
152. Missana T, Garcia-Gutiérrez M, Alonso U, Almendros-Ginesta O (2022) Nickel retention by calcium silicate hydrate phases: evaluation of the role of the Ca/Si ratio on adsorption and precipitation processes. *Appl Geochem* 137:105197
153. Pointeau I (2000) Etude mécanistic et modélisation de la rétention de radionucléides par les silicates de calcium hydratés (CSH) des ciments. PhD thesis, l'Université de Reims-Champagne-Ardenne, France
154. Ziegler F, Gieré R, Johnson C (2001) Sorption mechanisms of zinc to calcium silicate hydrate: Sorption and microscopic investigations. *Environ Sci Technol* 35:4556–4561
155. Lemire RJ, Berner U, Musikas C, Palmer DA, Taylor P, Tochiyama O (2013) Chemical thermodynamics of iron. OECD Publications, Paris
156. Lemire RJ, Taylor P, Schlenz H, Palmer DA (2020) Chemical thermodynamics of iron—part 2. OECD Publications, Paris
157. Kulik DA, Miron GD, Lothenbach B (2022) A structurally-consistent CASH plus sublattice solid solution model for fully hydrated C–S–H phases: thermodynamic basis, methods, and Ca–Si–H₂O core sub-model. *Cem Concr Res* 151:106585
158. Bourdoiseau JA, Sabot R, Jeannin M, Termemil F, Refait P (2012) Determination of standard Gibbs free energy of formation of green rusts and its application to the Fe(II–III) hydroxy-oxalate. *Colloid Surf A* 410:72–80
159. Rémazeilles C, Refait P (2008) Formation, fast oxidation and thermodynamic data of Fe(II) hydroxychlorides. *Corros Sci* 50:856–864
160. Snow CL, Smith SJ, Lang BE, Shi QA, Boerio-Goates J, Woodfield BF, Navrotsky A (2011) Heat capacity studies of the iron oxyhydroxides akaganeite (beta-FeOOH) and lepidocrocite (gamma-FeOOH). *J Chem Thermodyn* 43:190–199
161. Kulik DA, Wagner T, Dmytrieva SV, Kosakowski G, Hingerl FF, Chudnenko KV, Berner UR (2013) GEM-Selektor geochemical modeling package: revised algorithm and GEMS3K numerical kernel for coupled simulation codes. *Comput Geosci* 17:1–24
162. Hummel W, Berner U, Curti E, Pearson FJ, Thoenen T (2002) Nagra/PSI chemical thermodynamic data base 01/01, Universal Publishers/uPUBLISH.com, USA, also published as Nagra Technical Report NTB 02-16, Nagra, Wettingen



163. Thoenen T, Hummel W, Berner U, Curti E (2014) The PSI/Nagra chemical thermodynamic database 12/07. PSI Report 14-04. Paul Scherrer Institut, Villigen PSI
164. Fernandez A, Lothenbach B, Alonso M, Calvo J (2018) Thermodynamic modelling of short and long term hydration of ternary binders. Influence of Portland cement composition and blast furnace slag content. *Constr Build Mater* 166:510–521
165. Scholer A, Lothenbach B, Winnefeld F, Zajac M (2015) Hydration of quaternary Portland cement blends containing blast-furnace slag, siliceous fly ash and limestone powder. *CemConcr Comp* 55:374–382
166. De Weerd K, Lothenbach B, Geiker M (2019) Comparing chloride ingress from seawater and NaCl solution in Portland cement mortar. *Cem Concr Res* 115:80–89
167. De Weerd K, Plusquellec G, Revert A, Geiker M, Lothenbach B (2019) Effect of carbonation on the pore solution of mortar. *Cem Concr Res* 118:38–56
168. Ben Haha M, Lothenbach B, Le Saout G, Winnefeld F (2012) Influence of slag chemistry on the hydration of alkali-activated blast-furnace slag—Part II: effect of Al_2O_3 . *Cem Concr Res* 42:74–83
169. Lothenbach B, Bary B, Le Bescop P, Schmidt T, Letterier N (2010) Sulfate ingress in Portland cement. *Cem Concr Res* 40:1211–1225
170. Ma B, Fernandez-Martinez A, Wang KF, Madé B, Henocq P, Tisserand D, Bureau S, Charlet L (2020) Selenite sorption on hydrated CEM-V/A cement in the presence of steel corrosion products: redox vs nonredox sorption. *Environ Sci Technol* 54:2344–2352
171. Ma B, Fernandez-Martinez A, Madé B, Findling N, Markelova E, Salas-Colera E, Maffei TGG, Lewis AR, Tisserand D, Bureau S, Charlet L (2018) XANES-based determination of redox potentials imposed by steel corrosion products in cement-based media. *Environ Sci Technol* 52:11931–11940
172. De Windt L, Spycher N (2019) Reactive transport modeling: A key performance assessment tool for the geologic disposal of nuclear waste. *Elements* 15:99–102
173. Steefel CI, DePaolo DJ, Lichtner PC (2005) Reactive transport modeling: an essential tool and a new research approach for the Earth sciences. *Earth Planet Sci Lett* 240:539–558
174. Bildstein O, Claret F (2015) Stability of clay barriers under chemical perturbations. *Developments in Clay Science*. pp 155–188
175. Idiart A, Lavina M, Kosakowski G, Cochepin B, Meeussen JCL, Samper J, Mon A, Montoya V, Munier I, Poonosamy J, Montenegro L, Deissmann G, Rohmen S, Damiani LH, Coene E, Naves A (2020) Reactive transport modelling of a low-pH concrete/clay interface. *Appl Geochem* 115:104562
176. Jenni A, Mäder U (2021) Reactive transport simulation of low-pH cement interacting with Opalinus Clay using a dual porosity electrostatic model. *Minerals* 11:664
177. Kosakowski G, Berner U (2013) The evolution of clay rock/cement interfaces in a cementitious repository for low- and intermediate level radioactive waste. *Phys Chem Earth* 64:65–86
178. Ngo VV, Delalande M, Clement A, Michau N, Fritz B (2014) Coupled transport-reaction modeling of the long-term interaction between iron, bentonite and Callovo-Oxfordian claystone in radioactive waste confinement systems. *Appl Clay Sci* 101:430–443
179. Dagher HJ, Kulendran S (1992) Finite-element modeling of corrosion damage in concrete structures. *Ac Struct J* 89:699–708
180. Pantazopoulou SJ, Papoulia KD (2001) Modeling cover-cracking due to reinforcement corrosion in RC structures. *J Eng Mech-Asce* 127:342–351
181. Ozbolt J, Orsanic F, Balabanic G, Kuster M (2012) Modeling damage in concrete caused by corrosion of reinforcement: coupled 3D FE model. *Int J Fract* 178:233–244
182. Jamali A, Angst U, Adey B, Elsener B (2013) Modeling of corrosion-induced concrete cover cracking: a critical analysis. *Constr Build Mater* 42:225–237
183. Bossio A, Monetta T, Bellucci F, Lignola GP, Prota A (2015) Modeling of concrete cracking due to corrosion process of reinforcement bars. *Cem Concr Res* 71:78–92

Publisher's Note Springer Nature remains neutral with regard to jurisdictional claims in published maps and institutional affiliations.

